Numerical analysis of carrier multiplication mechanisms in nanocrystalline and bulk forms of PbSe and PbS

Kirill A. Velizhanin[*] and Andrei Piryatinski[†]

Center for Nonlinear Studies (CNLS), Theoretical Division, Los Alamos National Laboratory, Los Alamos, New Mexico 87545, USA

We report on a systematic numerical study of carrier multiplication (CM) processes in spherically symmetric nanocrystalline and bulk forms of PbSe and PbS representing the test bed for understanding basic aspects of CM dynamics. The adopted numerical method integrates our previously developed interband exciton scattering model and the effective mass based electronic structure model for the lead chalcogenide semiconductors. The analysis of CM pathways predicted by the interband exciton scattering model shows complete lack of their interference during the biexciton photogeneration. This allows us to interpret this process as a single impact ionization event and to explain a major contribution of the multiple impact ionization events during the phonon-assisted population decay into the total quantum efficiency (QE). We investigate the role of quantum confinement on QE and find that the reduction in the biexciton density of states (DOS) overruns weak enhancement of the Coulomb interactions leading to lower QE values in nanocrystals as compared to the bulk on the absolute photon energy scale. However, represented on the photon energy scale normalized by corresponding band gap energies, the trend in QE is opposite demonstrating the advantage of nanocrystals for the photovoltaic applications. Comparison to published experimental data allows us to interpret the observed features and to validate the applicability range of our model. Modeling of QE as a function of pulse duration shows weak dependence for the Gaussian pulses. Finally, comparison of the key quantities determining QE in PbSe and PbS demonstrates the enhancement of impact ionization rate in the latter materials. However, the fast phonon-assisted population decay in PbS nanocrystals can lead to experimentally observed reduction in QE as compared to PbSe nanocrystals.

I. INTRODUCTION

An ability to produce more than one electron-hole pairs (excitons) per single absorbed photon in semiconductor materials can potentially enhance the solar energy conversion efficiency in photovoltaic devices beyond the fundamental Shockley-Queisser limit.[1–8] In the literature, this process is referred to as Carrier Multiplication (CM) or multiple exciton generation, MEG, and has been extensively studied in the *bulk* semiconductors for decades.[9–13] Recent ultrafast optical studies of CM in semiconductor *nanocrystals* reported significantly higher quantum efficiency (QE) and much lower activation energy threshold (AET) as compared to the bulk materials on the photon energy scale normalized by the corresponding band gap values.[3,14–23]

These reports stimulated extensive experimental and theoretical studies of CM in the nanostructured materials in which the exciton dynamics is affected by quantum confinement. It was initially expected that the quantum confinement enhancement of Coulomb interactions between carriers could result in more efficient multiexciton production. Furthermore, a relaxation of the quasimomentum conservation constrains by breaking the translational symmetry should open additional pathways for CM and reduce the AET. Finally, the presence of phonon bottleneck in the nanocrystals should slow down the intraband phonon-assisted population decay and further increase the QE. However, subsequent reports claimed significantly lower QE and even the absence of CM in the nanocrystals.[24–27] This controversy possibly rises from experimental inaccuracy,[26,28] sample-to-sample variation in surface preparation,[29–34] and contribution from extraneous

effects such as photocharging.[35,36] The optical measurements of QE in bulk PbS and PbSe semiconductors[37] show that the *bulk* QE exceeds validated values in nanocrystals[25,35,36,38–40] if compared on the absolute photon energy scale.[37] However, due to confinement induced increase in the band gap energy, E_g, the benefits to photovoltaics is higher in nanocrystals than in bulk. The controversy calls for the development of new sensitive spectroscopic tools,[41,42] alternative photocurrent measurements,[43,44] and reassessment of the quantum confinement role in CM dynamics based on a unified theoretical model.[25,45]

Accepted theoretical models of CM are based on the many-body Coulomb interactions that correspond to the valence-conduction band transitions conserving total charge but not the number of electrons and holes.[46–48] In the exciton picture, this represents transitions between the exciton bands of different multiplicity. Hence, we will refer to these transitions below as the *interband exciton transitions*, and to the corresponding Coulomb interactions as the *interband Coulomb interactions*. Within adopted nomenclature, the *intraband Coulomb interactions* (i.e., restricted to an exciton band of a certain multiplicity) conserve the number of electrons and holes and determine the multiexciton interaction (e.g., binding) energy.

The simplest theoretical model initially developed to explain CM in bulk materials is the impact ionization impact ionization model.[49] It treats CM dynamics following high-energy photoexcitation as the lowest-order interband transitions whose rate is given by the Fermi's golden rule. This rate depends on the interband Coulomb matrix elements and the final multiple-carriers (e.g., biexciton) density of states (DOS).[50,51] The model has been further applied to interpret CM

dynamics in the nanocrystals along with various methods for the electronic structure calculations.

Franceschetti, An, and Zunger performed atomistic pseudopotential calculations of the impact ionization and Auger recombination rates in PbSe nanocrystals. Assuming the absence of the quasimomentum constraint and rapid growth of the biexciton DOS, they estimated low value ($\sim 2.2 E_g$) of AET after defining this quantity as the energy above which the impact ionization rate exceeds the Auger recombination one.[52] Rabani and Baer performed screened semiempirical pseudopotential calculations of the impact ionization rates in CdSe and InAs and found significant reduction of QE as the nanocrystal size increases. The observed trend makes CM already inefficient in the nanocrystals whose diameter is ~ 3 nm. The observation has been rationalized by strong size dependence of the interband Coulomb interactions and the trion DOS behavior.[53]

Using the semiempirical tight-binding model, Allan and Delerue performed extensive calculations for PbSe, PbSe, InAs, and Si nanocrystals.[54,55] They found that although the Coulomb interactions are enhanced by the quantum confinement, the quantum-confinement-induced reduction in the biexciton DOS facilitates *decrease* of the impact ionization rate and subsequently decrease of QE. The comparison of the impact ionization rates calculated in PbSe bulk and PbSe nanocrystals shows that the impact ionization rates in the nanocrystals does not exceed the bulk one.[54] Based on these calculations, the authors of Ref. [37] argue that the experimentally observed drop of QE in the nanocrystals can be attributed to the dominant effect of the reduced carriers' DOS. Lack of the phonon bottleneck, leads to the rapid intraband phonon-assisted relaxation that further reduces the QE.[54,55]

Schaller, Agranovich, and Klimov, first pointed out that in addition to impact ionization, the direct photogeneration of biexcitons can take place in nanocrystals through "virtual-exciton channel."[15] Subsequently, Rupasov and Klimov suggested that additional contribution to photogeneration QE can rise from the "vitual biexciton channel."[56] Using the effective mass model for the electronic structure of PbS and PbSe nanocrystals proposed by Kang and Wise,[57] the authors estimated the photogeneration QE and argued that this process provides the dominant contribution to the net QE in the nanocrystals. Recently, Silvestri and Agranovich, using the same model, performed detailed calculations for relatively small radii (i.e., 1.95 and 3 nm) PbSe nanocrystals.[58] They concluded that the contribution of the photogeneration processes in nanocrystals is much weaker than it was claimed before and clarified that the overestimated values of QE result from disregarding the effect of selection rules for the interband Coulomb matrix elements and the oscillator strength factors weighting optically allowed transitions. Here, we demonstrate that the absence of the interference between the photogeneration pathways and the presence of small size dispersion further decreases the photogeneration QE.

Another model describing the *coherent* photogeneration of biexcitons from the resonant exciton states, initially proposed by Shabaev, Efros, and Nozik considered an idealized five-level system,[59] and was subsequently refined to account for

the biexciton DOS effect.[60] Using the effective mass $\mathbf{k} \cdot \mathbf{p}$ Hamiltonian, the authors of Ref. [60] performed calculations for the small radii (i.e., 2 and 3 nm) PbSe nanocrystals, and found that dense biexciton DOS leads to the vanishing coherent oscillations between exciton and biexciton states. They also pointed out that efficient CM can be expected in the considered small nanocrystals. A drawback of the coherent superposition model is the lack of pure-dephasing effects and the inhomogeneous broadening, which as we demonstrate here play important role in the CM dynamics leading to smaller QE.

Finally, the *ab initio* calculations on small *clusters* ($\lesssim 1$ nm) revealed the role of strong Coulomb correlations and fast exciton-biexciton dephasing rates in the multiexciton photogeneration[61,62] and suggested additional contributions of the phonon-assisted Auger processes to CM.[63] The atomistic calculations mostly focused on impact ionization dynamics occurring during the population decay are limited to the small diameter ($\lesssim 3$ nm) nanocrystals. However, reported experimental studies consider larger nanocrystals with the diameter varying up to 10 nm. To close this gap and to perform a comparison with the bulk materials, an extrapolation procedure combined with atomistic calculations has been proposed.[64] For larger but still small diameter (~ 4–6 nm) nanocrystals, the photogeneration dynamics has been investigated with the help of an effective mass model.

Recently, we have published a letter summarizing the results of our numerical investigation on the direct photogeneration and population decay processes contributing to CM in the broad diameter range PbSe nanocrystals and in PbSe bulk.[65] The calculations employ our earlier proposed interband exciton scattering model[48] that recovers the models discussed above as various limiting cases and which we further parametrized using the Kang and Wise effective mass, $\mathbf{k} \cdot \mathbf{p}$, electronic structure model.[57,66] In the letter, we argue that in both cases of the photogeneration and population decay dynamics, the impact ionization is the main mechanisms of CM. This explains weak contribution of the direct photogeneration to the total quantum QE. Analyzing the scaling of the total QE with the nanocrystals size, we found that the nanocrystals QE plotted on the absolute energy scale does not exceed the bulk QE. This is in agreement with the reported experimental data and some theoretical studies and confirms that the quantum-confinement-induced reduction in the biexciton DOS leads to the decease of QE.

This paper discusses in great details the theoretical method and provides extended analysis of the numerical results summarized in Ref. [65]. In addition, we consider the effect of optical pump pulse duration on QE, and provide a comparative analysis of the key processes leading to CM in PbS and PbSe materials. The paper is organized as follows. In Sec. II, we review the weak Coulomb interaction limit of the interband exciton scattering model used for the numerical calculations, introduce a convenient quasicontinuous representation, and further discuss the details of the model parametrization. In Sec. III, an extensive analysis of our numerical results for PbSe nanocrystals is given. Comparison of PbSe and PbS is performed in Sec. IV. Section V concludes the paper by discussing limitations of the adopted model, providing a connection with experiment, and suggesting possible ways to enhance QE in the nanocrystals.

II. THEORETICAL MODEL AND NUMERICAL PARAMETRIZATION

The central quantity describing CM efficiency is QE, which can be calculated as[3]

$$QE = \frac{2N_{xx} + N_x}{N_{xx} + N_x}. \tag{1}$$

Here, N_x and N_{xx} are the total exciton and biexciton populations, respectively, produced by a single absorbed photon in the limit of vanishing pump fluence. In general, QE depends on the delay time measured from the center of the pump pulse. By taking into account that the photogeneration process occurs on subpicosecond and the population decay on picosecond time scales, the photogeneration QE can be attributed to the N_x and N_{xx} values at times longer than the pulse duration but much shorter than the population decay time. The total QE is attributed to the exciton and biexciton band-edge population values on a time scale longer than the population decay time but much shorter than the Auger recombination time for the *band-edge* biexciton. This quantity is typically determined in experiment.[35] A complimentary quantity, often used to describe CM, is the biexciton quantum yield, $\eta_{xx} = QE - 1$, defined as a number of biexcitons produced per single absorbed photon.

Next, we review the weak Coulomb limit of the interband exciton scattering model[48] also outlined in Appendix A. This approach has been implemented to calculate the time evolution of the exciton and biexciton populations in Eq. (1). We further introduce the quasicontinuous frequency representation, which is convenient to analyze the quantum confinement signatures and the size scaling of the quantities determining QE in transition from a nanocrystal to the bulk limit. Finally, we discuss the model parametrization used in our numerical calculations of QE for PbSe and PbS materials.

A. Biexciton photogeneration and population relaxation model

Derivations of the expressions for the exciton, $n_a^{x(0)}$, and biexciton, $n_k^{xx(2)}$, populations generated by optical ultrafast pump pulse are given in Appendix A. Accordingly, in the weak Coulomb interaction limit, the leading contribution to the photogenerated population of the ath exciton state is[48]

$$n_a^{x(0)} = \left| \mu_{a0}^x \right|^2 \mathcal{I}(\omega_a^x - \omega_{pm}), \tag{2}$$

where μ_{a0}^x is transition dipole moment between the ground state, $|x_0\rangle$, (i.e., filled valence band) and an exciton state $|x_a\rangle$, projected on the direction of linearly polarized pump pulse.

$$\mathcal{I}(\omega_a^x - \omega_{pm}) = \frac{2}{\hbar^2} \int_{-\infty}^{\infty} dt' \int_0^{\infty} dt_1 e^{-\gamma_a^x t_1} \\ \times \cos\left[(\omega_a^x - \omega_{pm})t_1\right] \mathcal{E}_{pm}(t') \mathcal{E}_{pm}(t' - t_1), \tag{3}$$

is the pulse self-convolution function depending on the exciton state transition frequency ω_a^x and dephasing rate γ_a^x. The pump pulse is characterized by the envelope electric field amplitude $\mathcal{E}_{pm}(t)$ determining the temporal profile of the pulse, and the central frequency ω_{pm}. In our calculations,

we used the Gaussian form of the pulse envelope function, $\mathcal{E}_{pm}(t) = \mathcal{E}_{pm}^{(0)} e^{-t^2/2\tau_{pm}^2}$, with the peak value $\mathcal{E}_{pm}^{(0)}$ and pulse duration defined as the temporal variance of the envelope, τ_{pm}. (The subscript pm is used to designate that the introduced quantities describe the optical pump pulse.) For the pulses longer than typical dephasing time, $\tau_{pm} \gg 1/\gamma$, the continuous wave limit is recovered and the pulse self-convolution function becomes proportional to the Lorentzian line shape function.

According to Appendix A, the photogenerated population of the kth biexciton state is

$$n_k^{xx(2)} = \sum_{a \geqslant 1} \left| \Lambda_{k,a}^{xx,x} \mu_{a0}^x \right|^2 \mathcal{I}(\omega_a^x - \omega_{pm}) \\ + \left| \sum_{a \geqslant 1} \Lambda_{k,a}^{xx,x} \mu_{a0}^x + \sum_{l \geqslant 1} \mu_{kl}^{xx} \Lambda_{l,0}^{xx,x} \right|^2 \mathcal{I}(\omega_k^{xx} - \omega_{pm}), \tag{4}$$

where μ_{kl}^{xx} is the intraband transition dipole between the biexciton states $|xx_k\rangle$ and $|xx_l\rangle$, and

$$\Lambda_{k,a}^{xx,x} = \frac{V_{k,a}^{xx,x}}{\hbar\left[\omega_k^{xx} - \omega_a^x + i\gamma_{k,a}^{xx,x}\right]}, \tag{5}$$

describes the transition amplitude associated with the single (Born) scattering event between exciton sate $|x_a\rangle$, and biexciton state $|xx_k\rangle$. The quantity $\Lambda_{l,0}^{xx,x}$, also entering Eq. (4), is the transition amplitude between the ground state $|x_0\rangle$ ($\omega_0^x = 0$) and biexciton state $|xx_l\rangle$. $V_{k,a}^{xx,x}$ is the interband Coulomb matrix element in the exciton representation giving rise to the interband scattering, and $\gamma_{k,a}^{xx,x}$ is the interband dephasing rate. The pulse self-convolution function $\mathcal{I}(\omega_k^{xx} - \omega_{pm})$, in Eq. (4), is defined by Eq. (3) but contains ω_k^{xx} and γ_k^{xx} instead of ω_k^x and γ_k^x, respectively.

Our numerical calculations show that the rapid sign variation of the interfering terms in Eq. (4) leads to their cancellation allowing us to write Eq. (4) as

$$n_k^{xx(2)} = \sum_{a \geqslant 1} \left| \Lambda_{k,a}^{xx,x} \mu_{a0}^x \right|^2 \mathcal{I}(\omega_a^x - \omega_{pm}) \\ + \sum_{a \geqslant 1} \left| \Lambda_{k,a}^{xx,x} \mu_{a0}^x \right|^2 \mathcal{I}(\omega_k^{xx} - \omega_{pm}) \\ + \sum_{l \geqslant 1} \left| \mu_{kl}^{xx} \Lambda_{l,0}^{xx,x} \right|^2 \mathcal{I}(\omega_k^{xx} - \omega_{pm}). \tag{6}$$

The resulting three *noninterfering* photogeneration pathways are illustrated in Fig. 1.

The first and the second pathways, given by the first and the second terms in Eq. (6), are shown in Figs. 1(a) and 1(b), respectively. These terms describe redistribution of the exciton oscillator strengths ($\sim |\mu_{0a}^x|^2$) between exciton and biexciton bands mediated by the interband Born scattering ($\Lambda^{x,xx}$). The first pathway [see Fig. 1(a)] involves the ground-to-exciton-state resonant optical transition and further scattering to the final biexciton states distributed around $\hbar\omega_{pm}$ according to the nonzero components of $\Lambda^{x,xx}$. We will refer to this process as the *indirect biexciton photogeneration* throughout this paper.[48] Figure 1(b) illustrates the second pathway, where the exciton is virtual and final biexciton state is in resonance with the optical pulse. Thus this pathway will be refereed to as the
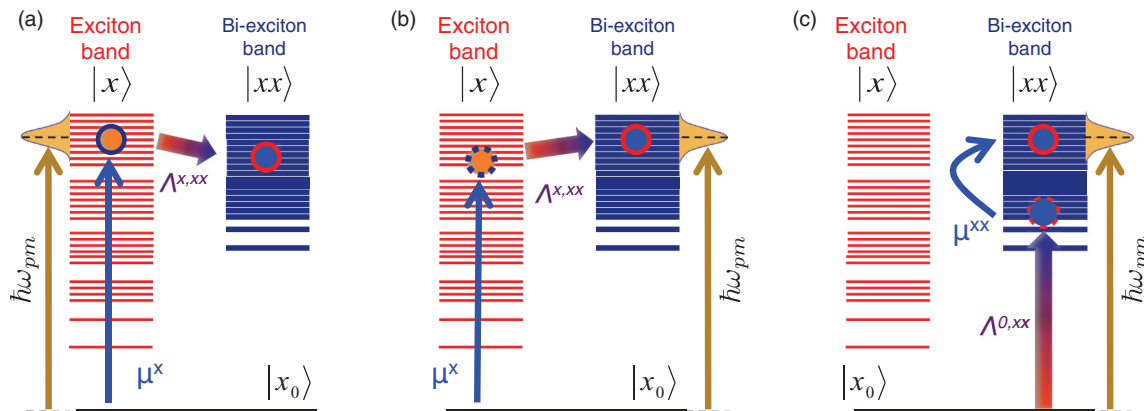
FIG. 1. (Color online) Noninterfering biexciton photogeneration pathways associated with the weak Coulomb limit. (a) Indirect biexciton photogeneration via exciton states. (b) Direct biexciton photogeneration via virtual exciton states. (c) Direct biexciton photogeneration via biexciton states. (See details in the text.)

direct biexciton photogeneration via virtual exciton states.[15] The third pathway [see Fig. 1(c)] consists of Born scattering between the ground and biexciton ($\Lambda^{0,xx}$) states stabilized by the intraband dipole transition, μ^{xx}. Accordingly, the final biexciton state is in resonance with the optical pulse. This process, refereed to as the *direct biexciton photogeneration via biexciton states*,[56] becomes prohibited in the bulk limit by the momentum conservation constraint for optical valence-conduction band transitions.

Equations (2)–(6) fully describe the exciton and biexciton populations prepared by the pump pulse. We use them for the numerical evaluation of the photogenerated exciton, $N_x = \sum_a n_a^x$, and biexciton, $N_{xx} = \sum_k n_k^{xx}$, populations and subsequently the QE [see Eq. (1)]. They also provide the initial conditions to model population decay dynamics using a set of rate equations.[48] Using this computational approach, our goal is to clarify the effect of quantum confinement on QE in transition from a nanocrystal to the bulk limit. Since the CM dynamics in nanocrystals takes place in the energy region characterized by high electron and hole DOS, we expect that the CM dynamics in the nanocrystals and bulk should have common features. Thus we intend to see how strongly these features are affected by the presence of the confinement potential.

Quantitatively, we are going to look at the interplay between the size scalings of the interband Coulomb interaction and exciton/biexciton DOS determining the QE variation in transition from nanocrystal to the bulk limit. First, we define the bulk limit as the thermodynamic limit: $V \to \infty$, $V/v \to \infty$, and $v = $ const., where V is a crystal volume, v is the unit cell volume, and the ratio V/v gives the number of unit cells in the crystal. Then Eqs. (2) and (6) and quantities determining the population decay should be represented in such a form that the effect of interband Coulomb interactions and exciton/biexciton DOS are clearly distinguished. This can be achieved by using the quasicontinuous energy representation defined below. Since some quantities of interest in the bulk limit have volume scaling, it is convenient to introduce associated intensive (i.e., volume independent in the bulk limit) variables. Their deviation from the well defined bulk values will provide us

with the convenient measure of the quantum confinement effects.

We start with the exciton and biexciton populations by recasting them to the quasicontinuous energy representation[67] by using the following transformations:[68]

$$n_x(\omega) = \sum_{a \geqslant 1} n_a^x \delta(\omega - \omega_a^x), \tag{7}$$

$$n_{xx}(\omega) = \sum_{k \geqslant 1} n_k^{xx} \delta(\omega - \omega_k^{xx}), \tag{8}$$

respectively. Both n_x and n_{xx} have linear scaling with the volume in the bulk limit. Therefore we eliminate the latter scaling by multiplying the total populations with the dimensionless prefactors v/V and end up with the following intensive quantities:

$$\tilde{N}_x = \frac{v}{V} \int_0^\infty n_x(\omega) d\omega, \tag{9}$$

$$\tilde{N}_{xx} = \frac{v}{V} \int_0^\infty n_{xx}(\omega) d\omega. \tag{10}$$

Although the prefactor v/V cancels out in the expression for QE (1), indicating that the latter quantity is indeed intensive, it is convenient to keep it in Eqs. (9) and (10) for consistency.

According to the arguments provided in Appendix B, we define the intensive exciton and biexciton DOS as

$$\rho_x(\omega) = \left(\frac{v}{V}\right)^2 \sum_a \delta(\omega - \omega_a^x), \tag{11}$$

$$\rho_{xx}(\omega) = \left(\frac{v}{V}\right)^4 \sum_k \delta(\omega - \omega_k^{xx}), \tag{12}$$

respectively. The associated *optically allowed* exciton and joint biexciton DOS can be defined as

$$\tilde{\rho}_x(\omega) = \left(\frac{v}{V}\right) \sum_a |\mu_{a0}^x|^2 \delta(\omega - \omega_a^x), \tag{13}$$

$$\tilde{\rho}_{xx}(\omega_1, \omega_2) = \left(\frac{v}{V}\right)^4 \sum_{kl} |\mu_{kl}^{xx}|^2$$
$$\times \delta(\omega_1 - \omega_k^{xx}) \delta(\omega_2 - \omega_l^{xx}), \tag{14}$$

respectively. These quantities carry information on the optical selection rules reducing number of states participating in the photogeneration process.

Our central quantity is the effective Coulomb interaction between the states within the frequency intervals $[\omega_1, \omega_1 + d\omega_1]$ and $[\omega_2, \omega_2 + d\omega_2]$ defined as the rms of the interband Coulomb matrix elements,[69]

$$V_{\text{eff}}^{x,xx}(\omega_1, \omega_2) = \left(\frac{V}{v}\right)^2 \left[\sum_{a,m} \left| V_{a,m}^{x,xx} \right|^2 \right.$$
$$\left. \times \frac{\delta(\omega_1 - \omega_a^x)\delta(\omega_2 - \omega_m^{xx})}{\sum_b \delta(\omega_1 - \omega_b^x) \sum_n \delta(\omega_2 - \omega_n^{xx})} \right]^{1/2}. \tag{15}$$

The related effective Coulomb term, connecting the ground and biexciton states, can also be defined as

$$V_{\text{eff}}^{xx}(\omega) = \left(\frac{V}{v}\right)^{3/2} \left[\sum_m \left| V_{0,m}^{x,xx} \right|^2 \frac{\delta(\omega - \omega_m^{xx})}{\sum_n \delta(\omega - \omega_n^{xx})} \right]^{1/2}. \tag{16}$$

As we show in Appendix B, the volume prefactor $(V/v)^2$ $[(V/v)^{3/2}]$ in Eq. (15) [Eq. (16)] corresponds to a finite effective Coulomb value in the bulk limit. Therefore the size scaling of such defined interaction with the nanocrystal diameter, d, provides a quantitative measure of the quantum confinement effects. In general, a deviation from the bulk value for the effective Coulomb interaction reflects the net result of the scaling of the Coulomb matrix elements with d, relaxation of the momentum conservation constraints, and the appearance of new selection rules associated with the symmetry of confinement potential.

Assuming the continuous wave excitation, the exciton and biexciton populations produced by the pump pulse can be obtained by substituting Eqs. (2) and (6) [along with Eq. (5)] into Eqs. (7) and (8), and further integrating over $d\omega$ as described in Eqs. (9) and (10), respectively. In this representation, the exciton population becomes simply proportional to the corresponding optically allowed DOS [see Eq. (13)],

$$\tilde{N}_x(\omega_{pm}) = \mathcal{A}\tilde{\rho}_x(\omega_{pm}), \tag{17}$$

where $\mathcal{A} = 2\pi^{3/2}\tau_{pm}\mathcal{E}_{pm}^{(0)\,2}/\hbar^2$. The biexciton population as a function of the pump frequency in the adopted representation reads

$$\tilde{N}_{xx}(\omega_{pm}) = \frac{\mathcal{A}}{\hbar^2} \int d\omega' \left[V_{\text{eff}}^{x,xx}(\omega_{pm},\omega') \right]^2 \frac{\tilde{\rho}_x(\omega_{pm})\rho_{xx}(\omega')}{(\omega' - \omega_{pm})^2 + \gamma^2}$$
$$+ \frac{\mathcal{A}}{\hbar^2} \int d\omega' \left[V_{\text{eff}}^{x,xx}(\omega',\omega_{pm}) \right]^2 \frac{\tilde{\rho}_x(\omega')\rho_{xx}(\omega_{pm})}{(\omega' - \omega_{pm})^2 + \gamma^2}$$
$$+ \frac{\mathcal{A}}{\hbar^2} \int d\omega' \left[V_{\text{eff}}^{xx}(\omega') \right]^2 \frac{\tilde{\rho}_{xx}(\omega'\omega_{pm})}{\omega'^2}, \tag{18}$$

and depends on the introduced above effective Coulomb interaction [see Eqs. (15) and (16)] as well as variously defined DOS [see Eqs. (12)–(14)]. As desired, Eq. (18) is volume independent and clearly distinguishes the contributions from the effective Coulomb interactions and the DOS. Accordingly, Eqs. (17) and (18) provide central expressions for

interpretation of our numerical results for the photogeneration QE provided in the subsequent section.

According to Appendix A, the phonon-assisted population relaxation dynamics is described by a set of kinetic equations [see Eqs. (A20)–(A22)]. We recast them to the quasicontinuous representation defined by Eqs. (7) and (8). This results in the following set of equations:

$$\dot{n}_x(\omega) = -k_{II}(\omega)n_x(\omega) + k_{AR}(\omega)n_{xx}(\omega)$$
$$- \int_0^\infty d\omega' \, \Gamma_x(\omega',\omega)n_x(\omega)$$
$$+ \int_0^\infty d\omega' \, \Gamma_x(\omega,\omega')n_x(\omega'), \tag{19}$$
$$\dot{n}_{xx}(\omega) = k_{II}(\omega)n_x(\omega) - k_{AR}(\omega)n_{xx}(\omega)$$
$$- \int_0^\infty d\omega' \, \Gamma_{xx}(\omega',\omega)n_{xx}(\omega)$$
$$+ \int_0^\infty d\omega' \, \Gamma_{xx}(\omega,\omega')n_{xx}(\omega'), \tag{20}$$

containing both the impact ionization and Auger recombination rates,

$$k_{II}(\omega) = \frac{2\pi}{\hbar^2} \left[V_{\text{eff}}^{x,xx}(\omega) \right]^2 \rho_{xx}(\omega), \tag{21}$$

$$k_{AR}(\omega) = \frac{2\pi}{\hbar^2} \left(\frac{v}{V}\right)^2 \left[V_{\text{eff}}^{x,xx}(\omega) \right]^2 \rho_x(\omega), \tag{22}$$

respectively. The shorthand notation, $V_{\text{eff}}^{x,xx}(\omega)$, stands for the diagonal component of the effective Coulomb term, i.e., $V_{\text{eff}}^{x,xx}(\omega) \equiv V_{\text{eff}}^{x,xx}(\omega,\omega)$. According to Eq. (21), the impact ionization rate is an intensive variable. In contrast, the Auger recombination rate [see Eq. (22)] vanishes in the the bulk limit as d^{-6}.

In the case when the impact ionization processes determine CM dynamics, the ratio of the impact ionization to Auger recombination rates,

$$\frac{k_{II}(\omega)}{k_{AR}(\omega)} = \left(\frac{V}{v}\right)^2 \frac{\rho_{xx}(\omega)}{\rho_x(\omega)}, \tag{23}$$

should determine QE. Since this ratio is proportional to the ratio of corresponding DOS, it has been proposed as a selection criterion for the materials showing efficient CM.[70] However, Eq. (23) clearly shows that besides the material-specific signatures given by the ratio of the *intensive* DOS, it also contains the volume scaling factor. Therefore, we argue that Eq. (23) can only be used for a material selection criterion, after the volume prefactor is eliminated.

The intraband relaxation rates, Γ_x and Γ_{xx}, in Eqs. (19) and (20) describe the phonon-assisted population decay. In the absence of the phonon bottleneck and in the region of high exciton DOS, it is expected that single-phonon processes dominate the exciton and biexciton intraband population decay. Accordingly, we calculate these quantities by using the following expression:[71,72]

$$\Gamma_\alpha(\omega',\omega) = \text{sign}(\omega' - \omega)\frac{2J_\alpha(|\omega' - \omega|)}{\exp[\hbar(\omega' - \omega)/k_B T] - 1}, \tag{24}$$

where $\alpha = x, xx$. $k_B T$ is thermal energy, and $J_\alpha(\Delta\omega)$ is the phonon spectral density approximated by the ohmic form with

exponential cutoff:

$$J_\alpha(\Delta\omega) = \lambda_\alpha \frac{\Delta\omega}{\omega_c} e^{-\Delta\omega/\omega_c}. \tag{25}$$

Here, the adjustable parameters are electron-phonon coupling, λ_α, with the constraint $\lambda_{xx} = 2\lambda_x$ and the phonon frequency cutoff, ω_c.

We found that the quasicontinuous representation of the kinetic equations [see Eqs. (19)–(25)] is more suitable for numerical integration. The solution of these equations with the initial conditions determined by the photogenerated populations [see Eqs. (2)–(6)] provides closed computational scheme that we use to determine the total QE. Next, we discuss the parametrization of the introduced model and some details on the adopted numerical techniques.

B. Model parametrization

An accurate knowledge of single-electron and hole wave functions is required to construct the exciton and biexciton states and to evaluate the transition dipoles and the interband Coulomb matrix elements. For this purpose, we adopt the effective mass $\mathbf{k} \cdot \mathbf{p}$ formalism, originally developed by Mitchell and Wallis,[73] and Dimmock[74] for the bulk lead chalcogenide semiconductors, and further advanced by Kang and Wise[57] for the spherically symmetric nanocrystals. The formalism is based on a four-band envelope function model explicitly taking into account spin-orbit interaction between valence and conduction bands. In considered PbSe and PbS materials, the band structure anisotropy is small and, therefore, is neglected in our calculations.

An electron and hole wave function obtained within this formalism reads

$$\Psi_i(\mathbf{r}) = \sum_{m=1}^{4} F_m^i(\mathbf{r}) u_m(\mathbf{r}). \tag{26}$$

Here, $u_m(\mathbf{r})$ is mth component of the bulk Bloch wave function associated with the band-edge states in L valley whose index, $m = 1, \ldots, 4$, denotes the bands.[73,74] The envelope eigenfunctions, $F_m^i(\mathbf{r})$, and the corresponding eigenenergies, $\hbar\omega_i$, are found by solving the $\mathbf{k} \cdot \mathbf{p}$ Hamiltonian eigenvalue problem with the infinite wall boundary condition, $F_i(|\mathbf{r}| = R) = 0$, at the surface of a spherical nanocrystal of radius R.[57] If $\hbar\omega_i > 0$ ($\hbar\omega_i < 0$), we identify the state as a conduction band electron (valence band hole) state. The eigenstate index represents a set of quantum numbers, $i = \{n, \pi, j, m\}$, such as a primary quantum number describing the number of the wave function nods, parity, total angular momentum, and its projection, respectively. In what follows, we will refer to the single-particle states, described by Eq. (26), as the Kang-Wise states. In the bulk limit, we set the envelope functions, $F_m^i(\mathbf{r})$, to the plane waves.

A natural way to introduce the exciton and biexciton states is to use the second quantization representation within the basis of the Kang-Wise states [see Eq. (C1)]. Taking into account that the electron-hole Coulomb interactions are weak compared to their kinetic energies (i.e., strong confinement regime), we introduce exciton and biexciton states as the following

configurations of *uncorrelated* electron-hole pairs:

$$|x_a\rangle = \hat{c}_q^\dagger \hat{d}_r^\dagger |x_0\rangle, \tag{27}$$

$$|xx_k\rangle = \hat{c}_p^\dagger \hat{c}_q^\dagger \hat{d}_r^\dagger \hat{d}_s^\dagger |x_0\rangle. \tag{28}$$

As introduced above, the ground state $|x_0\rangle$ is attributed to the fully filled valence band. An exciton (biexciton) energy in terms of the electron $\hbar\omega_p^e$ and the hole $\hbar\omega_q^h$ energies is simply: $\hbar\omega_a^x = \hbar\omega_q^e - \hbar\omega_r^h$ ($\hbar\omega_k^{xx} = \hbar\omega_p^e + \hbar\omega_q^e - \hbar\omega_r^h - \hbar\omega_s^h$). Note that the exciton index $a = \{p, q\}$ (biexciton index $k = \{pq, rs\}$) is a collection of two (four) sets of Kang-Wise quantum numbers.

The expressions used to calculate the dipole moments, μ_{a0}^x and μ_{kl}^{xx}, and the interband Coulomb matrix elements, $V^{x,xx}$, in Eqs. (2), (4), (5), (15), and (16) using the Kang-Wise basis set are given in Appendix C. Numerical calculations of the interband Coulomb Kang-Wise matrix elements are performed with the help of multipole expansion in terms of the Clebsch-Gordan coefficients. The dephasing rates for the *high excited states* are not available from experiment, and in our calculations we use some average value of $\hbar\gamma^x = \hbar\gamma^{xx}/2 = \hbar\gamma^{x,xx}/2 = 50$ meV. This value is consistent with the calculations performed on PbSe clusters.[61,77,78]

The numerical calculations of the photogenerated populations have been done according to Eqs. (2)–(5) including the first- and second-order corrections to Eq. (2) provided in Ref. 48. To account for the degeneracy of the exciton and biexciton states associated with the four equivalent L valleys, we multiply the right-hand side of Eqs. (2) and (4) by factors 4 and 16, respectively. This assumes that the intervalley Coulomb scattering processes are negligible. In most calculations, the pump pulse duration is set to $\tau_{pm} = 50$ fs, which is a typical value used in the experimental studies.[75]

The number of exciton and biexciton states to handle computationally is extremely high. Even for PbSe nanocrystals of moderate size ($d \sim 5$ nm), the number of the biexciton states with energies below $4E_g$ is $\sim 10^5$. In the bulk limit, the number of the exciton and biexciton states becomes infinite rendering the direct summation over these states in Eq. (4) impossible. Therefore, in both cases of finite-size nanocrystals and the bulk, we use the Monte Carlo sampling, which allows us to consider significantly larger nanocrystals than it was possible in the work of Silvestri and Agranovich.[58]

To perform numerical calculations of the population decay processes, we first evaluated the interband Auger recombination and impact ionization rates according to Eqs. (21) and (22). For this purpose, we smeared the delta functions in the effective Coulomb term [see Eq. (15)] and exciton/biexciton DOS [see Eqs. (11) and (12)] with the Lorentzian profiles containing the corresponding dephasing rates and used the Monte Carlo procedure to sum over the exciton and biexciton states. To evaluate the phonon-assisted population decay rates [see Eqs. (24) and (25)], we set the room-temperature value for $k_B T = 25$ meV and the cutoff energy to $\hbar\omega_c = 50$ meV. The electron-phonon coupling $\lambda_x = \lambda_{xx}/2$ was fit to reproduce the experimentally observed intraband population decay time in the range of $0.5 \leqslant \tau_{\text{ph}} \leqslant 5$ ps.[37,54] The kinetic equations [see Eqs. (19) and (20)] have been further numerically integrated on

the energy grid. All calculated observables are averaged over a nanocrystal ensemble with the Gaussian size distribution characterized by the standard deviation $\sigma = 5\%$.

III. INTERPLAY OF CM PATHWAYS IN PbSe

In this section, we discuss our numerical results for the photogeneration and population relaxation processes in the nanocrystalline and bulk PbSe. We clarify the effect of interplay between CM pathways and the effect of quantum confinement on QE. As mentioned above, QE depends on the interplay between DOS and effective Coulomb values scaling with the size of nancrystals. Therefore, to set the stage for further analysis, we start by considering these quantities.

The calculated energy dependence of the exciton and biexciton DOS [see Eqs. (11) and (12)] for different diameter PbSe nanocrystals and the bulk is shown in Figs. 2(a) and
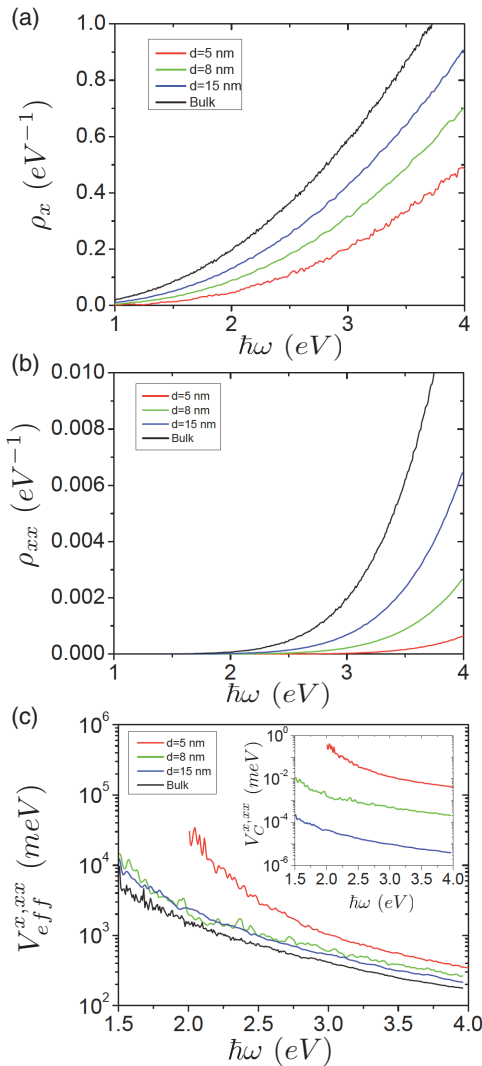

FIG. 2. (Color online) Energy dependence of (a) exciton and (b) biexciton DOS calculated for various diameter, d, PbSe nanocrystals and PbSe bulk. (c) The diagonal component of the effective Coulomb term. The inset shows actual interband Coulomb interaction in nanocrystals defined as the effective Coulomb term with the volume prefactor canceled, i.e., $V_C^{x,xx} = (V/v)^2 V_{\text{eff}}^{x,xx}$.

2(b), respectively. Obviously, the quantum confinement leads to the DOS reduction in the nanocrystals compared to the bulk. The energy dependence of the DOS follows power law. Specifically, for the bulk limit, we find that $\rho_x(\omega) \sim (\omega - \omega_g)^{2.2}$ and $\rho_{xx}(\omega) \sim (\omega - 2\omega_g)^6$ with $\hbar\omega_g = 0.28$ eV reflecting contributions of the nonparabolic regions of the electron/hole band structures. Even in the high-DOS regions where the bulk behavior is expected in nanocrystals, the DOS converges rather slowly to the limiting bulk values as the nanocrystal diameter increases.

The effective Coulomb interaction as a function of energy is plotted in Fig. 2(c) and follows power law behavior, $V_{\text{eff}}^{x,xx}(\omega) \sim \omega^{-5}$. According to the plot, the effective Coulomb interaction is only weakly enhanced by quantum confinement, except for the small diameter (i.e., $d = 5$ nm) nanocrystals. Specifically, the confinement results in a factor of two Coulomb enhancement for the nanocrystals with $d = 8$ nm as compared to the bulk. Therefore the scaling of the actual interband Coulomb interaction, i.e., $V_C = (v/V)^2 V_{\text{eff}}^{x,xx}$, in nanocrystals [inset to Fig. 2 (c)] in the region of high DOS should be dominated by the volume prefactor, i.e., $\sim d^{-6}$. However, we remind that the volume prefactor responsible for such dramatic scaling does not enter the quantities determining the QE except the Auger recombination rate [see Eqs. (17)–(22)].

A. Photogeneration QE

The photogeneration QE as a function of the absolute photon energy in nanocrystalline and bulk PbSe is shown in Fig. 3(a). According to the plot, the QE at fixed photon energy monotonically increases with the nanocrystal diameter but does not exceed the bulk value. In contrast, the QE plotted on the unitless photon energy scale [see Fig. 3(b)] shows the opposite trend useful for the photovoltaic applications. Since the absolute energy scale representation is more suitable to understand the physical mechanisms of photogeneration, we continue our analysis using this scale. First, we compare our calculations for small, $d = 5$ nm, nanocrystal with the calculations reported by Silvestri and Agranovich[58] for $d = 6$ nm PbSe nanocrystal. In Ref. 58, the size dispersion of the nanocrystals is set to 2% resulting in sharp peaks reaching QE ≈ 1.2. The increase in the dispersion to a realistic value of 5% [red solid line in Fig. 3(a)] washes out the peaks and reduces the QE to QE ~ 1.01.

Contributions of different pathways (see Fig. 1) to the biexciton photogeneration quantum yield, $\eta_{xx} = \text{QE} - 1$, are depicted in Fig. 4. First of all, we point out that for the energy region $\hbar\omega_{pm} > 1.5$ eV in which the biexciton DOS shows steep growth, the indirect biexciton photogeneration (black line) and the direct biexciton photogeneration via exciton state (red line), provide identical contributions. This behavior can be interpreted by looking at the related first and second terms in Eq. (18) in which the resonant nature of the denominator, $(\omega' - \omega_{pm})^2 + \gamma^2$, corresponds to the leading contribution of the diagonal component of the effective Coulomb term $V_{\text{eff}}^{x,xx}(\omega_{pm}) \equiv V_{\text{eff}}^{x,xx}(\omega_{pm}, \omega_{pm})$. Hence, the integral convolutions can be evaluated resulting in the identical two terms whose net contribution to the biexciton population
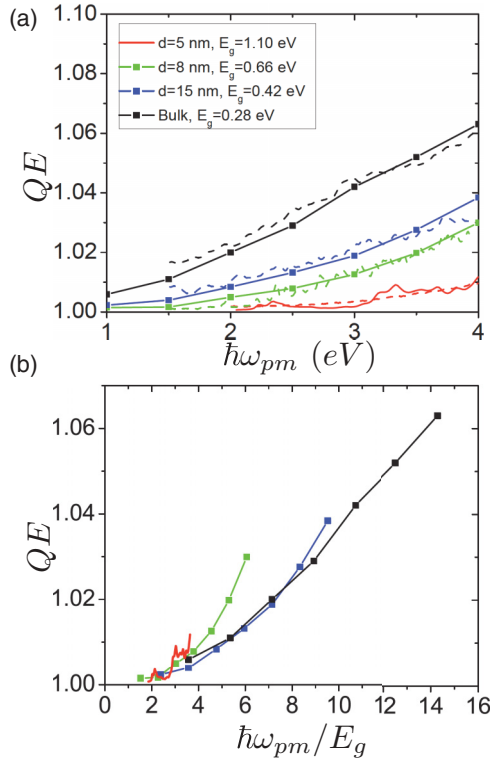
FIG. 3. (Color online) (a) The pump energy dependence of the photogeneration QE for various diameter, d, nanocrystalline and bulk PbSe plotted on the absolute pump energy scale. Solid lines represent the results obtained from numerically exact [see Eqs. (2)–(5)] calculations, and the dash indicates approximate calculations [see Eq. (30)] for $d = 5$, 8, 15 nm nanocrystals and the bulk using the effective dephasing rates $\hbar\gamma_{\text{eff}} = 50$, 40, 55, and 45 meV, respectively. (b) Solid lines from (a) plotted on the unitless pump energy scale (i.e., normalized by corresponding nanocrystals and bulk band gap energies E_g).

is

$$\tilde{N}'_{xx}(\omega_{pm}) = k_{II}(\omega_{pm})\tilde{N}_x(\omega_{pm})/\gamma_{\text{eff}}. \qquad (29)$$

Here, k_{II} is the impact ionization rate given by Eq. (21) and γ_{eff} is effective interband dephasing rate. The derived expression has a very clear physical interpretation: *the photogenerated biexciton population associated with the first and second pathways is a result of a single impact ionization event taking place on the dephasing time scale γ_{eff}^{-1} and following optical preparation of the exciton states.*[76]

The direct biexciton photogeneration via exciton states is manifested by the direct dependence of the biexciton DOS on ω_{pm} in the second term of Eq. (18). As a result, for $\hbar\omega_{pm} < 1.5$ eV, this contribution (red line in Fig. 4) drops quickly. Accordingly, $\hbar\omega_{pm} = 1.5$ eV can be identified as the AET for the photogeneration processes in $d = 15$ nm nanocrystals. In contrast, the indirect biexciton photogeneration (black line in Fig. 4) is resonant at exciton states, and decreases relatively slow for $\hbar\omega_{pm} \lesssim 1.5$ eV. According to the first term in Eq. (18), this behavior reflects the behavior of the off-diagonal effective Coulomb component $V_{\text{eff}}^{x,xx}(\omega', \omega_{pm})$ at $\hbar\omega' \lesssim 1.5$ eV.

Figure 4 clearly shows that direct biexciton photogeneration via biexciton states (green line) has negligibly small contri-
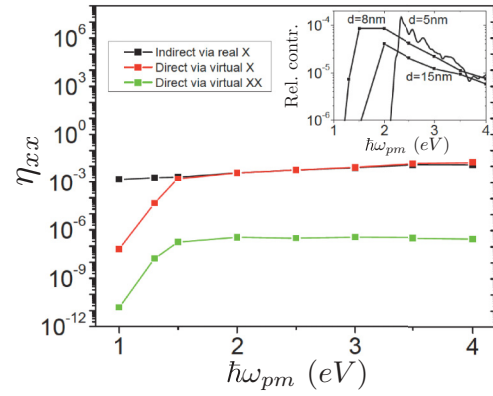

FIG. 4. (Color online) Contributions of the photogeneration pathways to the biexciton quantum yield calculated for $d = 15$ nm PbSe nanocrystal. Black and red lines show the contributions of the two components associated with the first two pathways schematically shown in Figs. 1(a) and 1(b), respectively. The green line shows the contribution of the third pathway illustrated in Fig. 1(c). The inset presents the relative contribution of the third pathway to the total photogeneration quantum yield in various size nanocrystals.

bution compared to the other terms. The inset shows that the relative contribution (i.e., normalized per total photogeneration QE) of the latter pathway for all considered nanocrystal sizes is small and has tendency to decrease with the nanocrystal size growth and further vanish in the bulk limit. This contribution becomes small due to the strong off-resonant nature of the ground state to biexciton state effective Coulomb term [see Eq. (16)] entering the third term in Eq. (18).

The small contribution of the last pathway leads us to an important conclusion that *the photogeneration QE is fully determined by a single impact ionization event occurring on the dephasing time scale*. According to Eqs. (1) and (29), this QE can be approximated by the following simple expression:

$$QE(\omega_{pm}) = \frac{2k_{II}(\omega_{pm}) + \gamma_{\text{eff}}}{k_{II}(\omega_{pm}) + \gamma_{\text{eff}}} \approx 1 + \frac{k_{II}}{\gamma_{\text{eff}}}, \qquad (30)$$

where k_{II} is the impact ionization rate given by Eq. (21) and γ_{eff} is the effective interband dephasing rate. Note that the optical selection rules do not enter Eq. (30). The approximate form of QE given in Eq. (30) is quite general, since the approximation is based on a general fact of weak interband Coulomb interaction. To verify this relation, we calculated the QE using Eqs. (21) and (30) and compare the results (dashed lines) in Fig. 3(a). The dashed lines well reproduce the trends in the behavior of the associated solid lines confirming the validity of the approximation. Observed small discrepancies are due to the numerical noise, phenomenological origin of the effective dephasing rate neglecting its frequency dependence, and neglect of the correlations between the effective Coulomb and DOS fluctuations during the nanocrystal ensemble averaging.

Both *direct* biexciton photogeneration pathways via exciton and biexciton states have been studied before.[15,56,58] The *indirect* biexciton generation as we demonstrated above is also important and should not be omitted. Initial studies of the photogeneration pathways[15,56] also based on the Kang-Wise
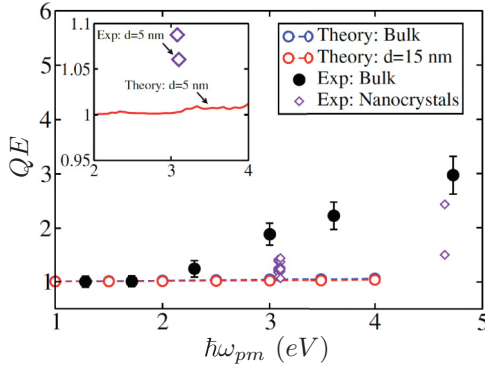
FIG. 5. (Color online) Calculated photogeneration QE as a function of pump energy for PbSe nanocrystal of $d = 15$ nm and PbSe bulk. For comparison, we also show experimentally measured total QE in PbSe nanocrystals[35] with the diameter varied in the range of $5 \leqslant d \leqslant 8$ nm and in the bulk.[37] The inset shows calculated QE for PbSe nanocrystal of $d = 5$ nm on extended pump energy scale compared to the experimentally measured total QE for the same size nanocrystal.

parametrization reported significantly larger QE compared to our results and the results report in Ref. 58. The cause of the overestimate is the disregard of the Coulomb coupling selection rules and the oscillator strengths factors weighting optically allowed transitions.[58] Next, we show that the interference related power-scaling of the DOS not accounted for in the previous studies further leads to a significant reduction in the photogenerated QE.

Provided, the terms in Eq. (4) associated with the direct biexciton photogeneration processes via exciton and biexciton states are interfering *constructively*, one can show that associated biexciton populations scale as $[\rho_x']^2 \rho_{xx}$ and $[\rho_{xx}']^2 \rho_{xx}$, respectively. This is exactly the case considered in Refs. 15 and 56. Here, ρ_x' (ρ_{xx}') is DOS for the intermediate exciton (biexciton) states and ρ_{xx} is the biexciton DOS at the pump frequency. Since we found that there is *no interference* between the photogeneration pathways, the first two terms in Eq. (18) scale as $\rho_x' \rho_{xx}$, and the last one as $\tilde{\rho}_{xx} \sim \rho_{xx}' \rho_{xx}$. The latter, linear dependence on the intermediate exciton and biexciton DOS versus the former, quadratic one[15,56] significantly decreases the biexciton photogeneration quantum yield and, in fact, allows us to interpret the photogeneration dynamics as a single impact ionization event [see Eq. (29)]!

In Fig. 5, we compare the experimentally measured total QE[35,37] with the calculated photogeneration QE. The comparison with experimental data for nanocrystals is possible only at the photon energy fixed at $\sim$3.1 eV, where the vertical aligned diamonds represent the QE measured for the nanocrystals whose diameters vary in the range between 5 and 8 nm. The comparison shows that for the bulk and for the nanocrystals of comparable diameter the experimentally measured total QE significantly exceeds the calculated photogeneration QE. Accordingly, we conclude that the biexciton photoexcitation along does not explain the experimentally observed QE values. Next, we investigate the contribution of the impact ionization events to the total QE taking place during the phonon-assisted population decay.
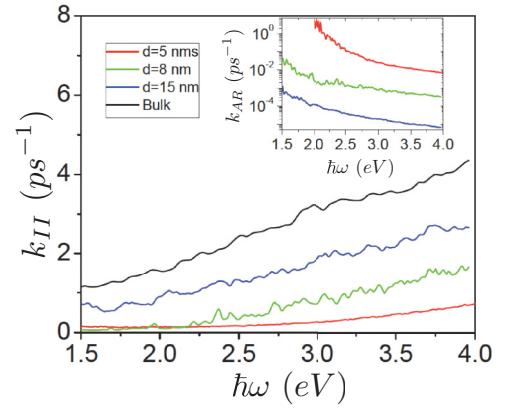

FIG. 6. (Color online) Energy dependence of the calculated impact ionization rates in PbSe nanocrystals of different diameter and in PbSe bulk. The inset shows associated Auger recombination rates calculated for the nanocrystals using [see Eq. (23)].

B. Effect of population decay and pump pulse duration on total QE

Central quantity defining QE during the population decay (and as shown above during the photogeneration event as well) is the impact ionization rate [see Eq. (21)]. Figure 6 shows the calculated energy dependence of the impact ionization rate for the nanocrystalline and bulk PbSe. According to the plot, the rate scales linearly at energies about 0.5 eV higher than AET. The scaling directly follows from Eq. (21) if one substitutes there the effective Coulomb, $V_{\text{eff}}^{x,xx}(\omega) \sim \omega^{-5}$, and biexciton DOS, $\rho_{xx}(\omega) \sim (\omega - 2\omega_g)^6$, whose scalings were determined from Fig. 2. In the literature, quadratic and even higher power scalings of the impact ionization rate are obtained *near* the AET. As proposed in Refs. 51, 79, and 80 such scalings solely follow from the DOS behavior. However, these theories do not account for the long-range interband Coulomb corrections at the energies higher than AET. As we show in Appendix C, the first nonvanishing $\mathbf{k} \cdot \mathbf{p}$ contribution to the matrix elements of the interband Coulomb term yields an additional factor $\omega^{-1/2}$. As a result, one gets $k_{II}(\omega) \sim (\omega - \omega_0)^2/\omega \sim \omega$ at $\omega \gg \omega_0$, which is in agreement with our numerical calculations.

According to Fig. 6, the impact ionization rate increases as the nanocrystal diameter increases but does not exceed the bulk values. This observation is a result of the *weak* effective Coulomb enhancement in the nanocrystals as observed in Fig. 2(c). In agreement with the previously reported studies,[37] we find that this enhancement is fully suppressed by the reduction in the biexciton DOS [see Fig. 2(b)]. As we already pointed out, strong size scaling of the actual interband Coulomb interaction is determined by the volume prefactor $(v/V)^2$, which does not enter the impact ionization rate, and therefore has no effect on the rate.

In contrast, the volume prefactor appears in the expression for the Auger recombination rate [see Eq. (22)], and as we show in the inset to Fig. 6, makes this effect negligible. On the frequency scale, the Auger recombination rate drops as $k_{\text{AR}} \sim \omega^{-3}$ further decreasing its contribution to QE at high energies. As a result, the only region where the Auger recombination processes are significant is near the band edge. However, this region has no contribution to QE, and we conclude that the
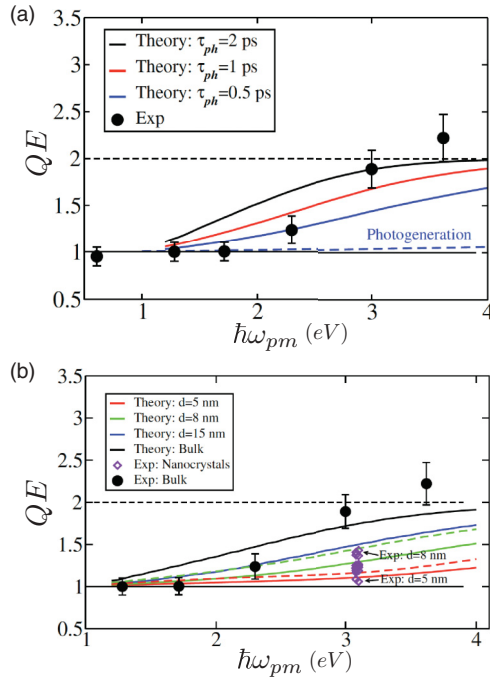
FIG. 7. (Color online) Pump energy dependence of the total QE in PbSe. (a) Calculations performed for bulk PbSe using various population decay times, $\tau_{\rm ph}$. Experimental data from Ref. 37 are shown for comparison. (b) Calculations for both nanocrystals and bulk using $\tau_{\rm ph} = 1$ ps (solid lines) and $\tau_{\rm ph} = 2$ ps (dash). For comparison, the experimental data from Refs. 35 and 37 are plotted in diamonds and dots, respectively.

Auger recombination processes can be neglected in the present analysis.

Since the Auger recombination processes are weak, efficient CM during the population decay is expected if the impact ionization rates are comparable to or higher than the phonon-assisted population decay rates. To evaluate the upper boundary for QE in nanocrystals, we first calculate total QE in bulk PbSe for typical population decay times $\tau_{\rm ph} = 0.5, 1.0$, and 2 ps. The results are plotted on the pump energy scale in Fig. 7(a) and also compared with published experimental data. In general, the calculations reproduce the experimental trends and provide the best fit at $\tau_{\rm ph} = 1.0$ ps. The discrepancy between theory and experiment in the interval $1.0 < \hbar\omega_{pm} < 3.5$ eV is due to the phenomenological nature of the phonon-assisted relaxation model that lacks exact knowledge on the spectral dependence of the electron-phonon coupling and phonon DOS. Above 3.5 eV, the effect of triexciton generation and possibly contribution from the higher energy bands take place. Hence our theory is valid below this energy value.

For comparison, the contribution of the photogeneration processes to the total QE is shown in Fig. 7(a). Its small contribution can be explained by the fact that the photogeneration pathways reduce to a *single* impact ionization event taking place on the short (subpicosecond) dephasing time scale [see Eq. (30)]. In contrast, the population decay dynamics occurs on a much longer (picosecond) time scale allowing for the *multiple* impact ionization events that make major input into the total QE.
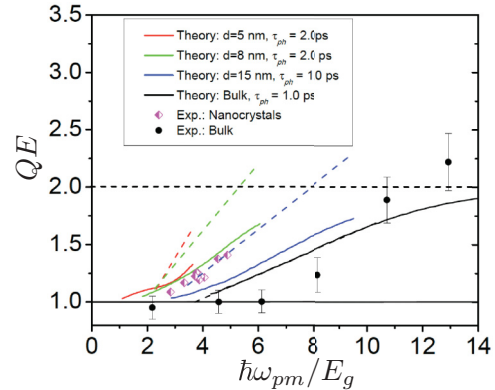

FIG. 8. (Color online) Comparison of the calculated total QE for selected $\tau_{\rm ph}$ and experimental data from Fig. 7(b) plotted on the unitless pump energy scale (i.e., normalized per corresponding band gap energy E_g). Dashed lines are extrapolation of the solid lines linear regions to determine the AET values (see Table I).

Comparison of the calculated total QE in both nanocrystalline and bulk PbSe with experimental results[35,37] is shown in Fig. 7(b). The total QE dependence on the nanocrystals diameter both in theory and experiment follows the same trend as the impact ionization rate. Solid lines in Fig. 7(b) show QE calculated for $\tau_{\rm ph} = 1.0$ ps, which gives the best fit for the bulk. However, taking into account that the upper values of the measured QE in the nanocrystals are associated with their diameter, $d = 8$ nm, we had to increase their relaxation time up to $\tau_{\rm ph} = 2$ ps (blue dash). This value gives better agreement with the experiment and can be rationalized by the quantum-confinement-induced increase of the level spacing.[81] The values of the population decay times determined above are also in good agreement with those obtained in earlier reported theoretical works.[54,64]

Determination of AET is convenient to perform using the unitless energy scale, i.e., the pump energy normalized per corresponding E_g of nanocrystals or the bulk. Figure 8 presents the same curves as in Fig. 7(b) for selected $\tau_{\rm ph}$, now, plotted on the unitless scale. Dashed lines extrapolate the linear portion of the curves to the energies below 3.5 eV. Their intercept points with the horizontal, $QE = 1$, line provide the AET values. The deviation from linear behavior at low energy ends and apparent CM below the energy conservation threshold, $2E_g$ (red and green curves) are merely due to the ensemble averaging included into our calculations.[82]

The calculated values of AET are summarized in Table I. For the nanocrystals with $d = 5, 8$ nm, the calculated AET $\approx 2.2E_g$ is in excellent agreement with the experiment.[35]

TABLE I. AET in PbSe nanocrystals and bulk calculated as the intercept point between dashed lines and the solid horizontal line at $QE = 1$ in Fig. 8.

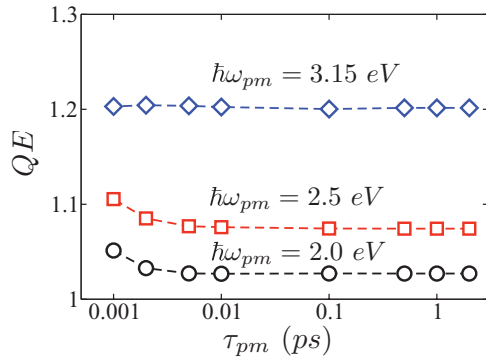| PbSe	d (nm)	E_g (eV)	AET/E_g	AET (eV)
Nanocrystal	5	1.10	2.3	2.5
Nanocrystal	8	0.66	2.2	1.5
Nanocrystal	15	0.42	3.3	1.4
Bulk	∞	0.28	3.7	1.0

FIG. 9. (Color online) Calculated dependence of the total QE for PbSe nanocrystal of $d = 8$ nm on the pump pulse duration, τ_{pm}. The population decay time is set to $\tau_{ph} = 1$ ps.

Furthermore, the *photogeneration* AET $= 1.5$ eV for the nanocrystals with $d = 15$ nm (see Sec. III A, Fig. 4) is close to the value of 1.4 eV given in Table I. This presents an additional indication of the "pure" impact ionization nature of CM processes including the photogeneration. For the bulk, however, there is a disagreement between the calculated, $3.7E_g$, and experimentally observed, $6E_g$, AET.[37] The discrepancy is related to the phenomenological nature of the adopted phonon-assisted relaxation model. Getting back to Fig. 7(a), one can clearly see that the best fit to the initial rise of QE is due to $\tau_{ph} = 0.5$ ps. However, for $\tau_{ph} = 1$ ps used to evaluate the AET, the model does not accurately reproduce the initial slope and gives the underestimated values of AET.

All calculations discussed above are performed for the continuous wave pulses typically used in the ultrafast spectroscopic studies. However, an estimated solar light correlation time is about 5 fs. Hence, in light of photovoltaic applications, it is natural to calculate QE as a function of the pump pulse duration τ_{pm}. Such a dependence evaluated for various photon energies, $\hbar\omega_{pm}$, is shown in Fig. 9. First of all, we notice that the continuous wave regime is reached at $\tau_{pm} > 10$ fs. For $\tau_{pm} < 10$ fs, the QE at $\hbar\omega_{pm} = 3.15$ eV has no variation whereas QE at the lower energies show insignificantly small increase. The observed weak dependence of QE on the pulse duration suggests that, for the Gaussian pulses, the expected increase in the QE due to the increase in the pulse duration is equally compensated by the reduction in the number of states populated by the pulse whose spectral width is narrowed.

IV. COMPARISON OF QE IN PbS and PbSe

Both PbS and PbSe have electronic structures described by the same Kang-Wise effective mass model with some different parameters.[57] This implies that our conclusions on the interplay between the CM pathways in PbSe fully apply to PbS nanocrystalline and bulk materials. In this section, we perform a comparison of the key quantities such as exciton/biexciton DOS, effective Coulomb terms, the impact ionization rates, and the resulting QEs calculated for these semiconductors. Our numerical tests show that these quantities are weakly affected by the differences in the Kane momentum and the unit cell volume. Hence, the dominant contributions come from the interplay between the band gap energies, carriers effective masses, and dielectric constants.

Figures 10(a) and 10(b) clearly show that both the exciton [see Eq. (11)] and biexciton [see Eq. (12)] DOS in bulk PbS exceed the corresponding DOS in PbSe across the spectral range of interest. Compared to PbSe ($E_g = 0.28$ eV), PbS has a larger band gap energy ($E_g = 0.41$ eV) and heavier carrier effective masses.[57] In order to isolate the band gap effect, we plot the PbSe DOS calculated with the band gap energy replaced by that of PbS (red dash). This replacement results in reduction of the DOS values (red dash). Hence, the major contribution to the steeper growth of the exciton and biexciton DOS in PbS comes from the heavier effective masses.

Figure 10 (c) compares the effective Coulomb terms, $V_{eff}^{x,xx}$ [see Eq. (15)], calculated for bulk PbSe and PbS. In contrast to the DOS, the effective Coulomb interaction in PbS is weaker
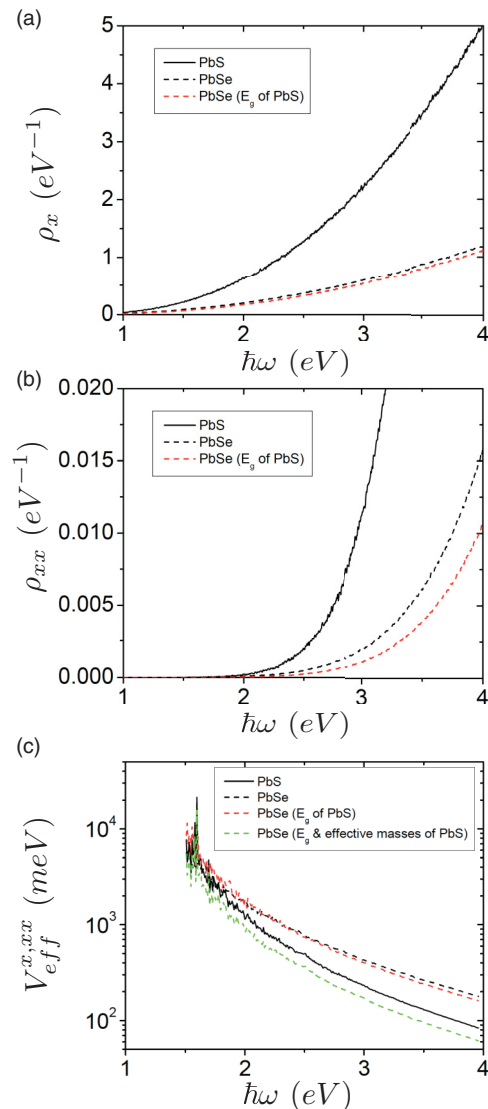

FIG. 10. (Color online) Energy dependence of (a) the exciton DOS, (b) the biexciton DOS, and (c) the effective Coulomb term in bulk PbS (solid black) and PbSe (dashed black). In all panels, red lines show the corresponding quantities calculated using PbSe parameters except for the band gap energy replaced with that of PbS. In (c), green line shows the effective Coulomb term calculated for PbSe with both band gap energy and the effective masses substituted with their corresponding PbS values.
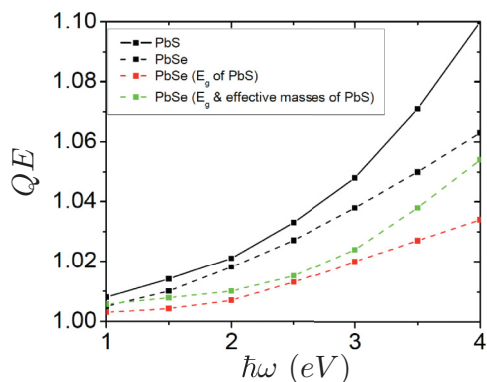
FIG. 11. (Color online) Energy dependence of the photogeneration QE in the bulk PbS (solid black) and PbSe (dashed black). Red (green) line shows the QE calculated for PbSe with the band gap energy (band gap energy and the effective masses) replaced with that (those) of PbS.

than that in PbSe. To understand the trends, we alter the PbSe band gap value in the same way as for the DOS and observe small reduction in $V_{\mathrm{eff}}^{x,xx}$ (red dash). Altering the effective masses of PbSe with those of PbS, significantly reduces the $V_{\mathrm{eff}}^{x,xx}$, i.e., lowers the green dash curve below black solid one ($V_{\mathrm{eff}}^{x,xx}$ in PbS). The gap between these curves is purely due to the difference in the dielectric constants which in PbS ($\epsilon = 17$) is lower than in PbSe ($\epsilon = 23$). Therefore, the lighter effective masses in PbS make a major contribution to the reduction of $V_{\mathrm{eff}}^{x,xx}$ values in PbS compared to PbSe.

Next, we compare the photogeneration QE in bulk PbS and PbSe plotted in Fig. 11. The plot also shows photogeneration QE values for PbSe with the band gap energy and effective masses altered in the same way as in the case of the effective Coulomb interaction. [The color code is the same as in Fig. 10(c).] By taking into account the linear dependence of the photogeneration QE on the impact ionization rate [see Eq. (30)], one can conclude that the trends in the behavior of the QE are a result of the interplay between the trends in the biexciton DOS and effective Coulomb term shown in Figs. 10(b) and 10(c), respectively. Specifically, the lower dielectric constant of PbS contributes to the increase in the photogeneration QE and the competing effect of the lighter effective masses on the DOS and $V_{\mathrm{eff}}^{x,xx}$ results in additional increase of the QE in bulk PbS. This net increase fully overruns the reductions associated with the band gap decrease making the photogeneration QE and the impact ionization rate [see Fig. 12(a)] in bulk PbS more efficient than in bulk PbSe.

To demonstrate that the size quantization does not change the trends, we plot the impact ionization rate calculated for PbS and PbSe nanocrystals and the bulk in Fig. 12(a). It is clear from the plot that the PbS impact ionization rate always exceeds the PbSe impact ionization for identical in diameter nanocrystals and for the bulk. Similar to PbSe, the PbS impact ionization rate monotonically increases with the nanocrystal diameter but does not exceed the bulk values. Finally, in Fig. 12(b), we plot the total QE in PbS and PbSe nanocrystals and the bulk calculated using *the same* population decay time, $\tau_{\mathrm{ph}} = 1.0$ ps. The trends are the same as in Fig. 12(a)
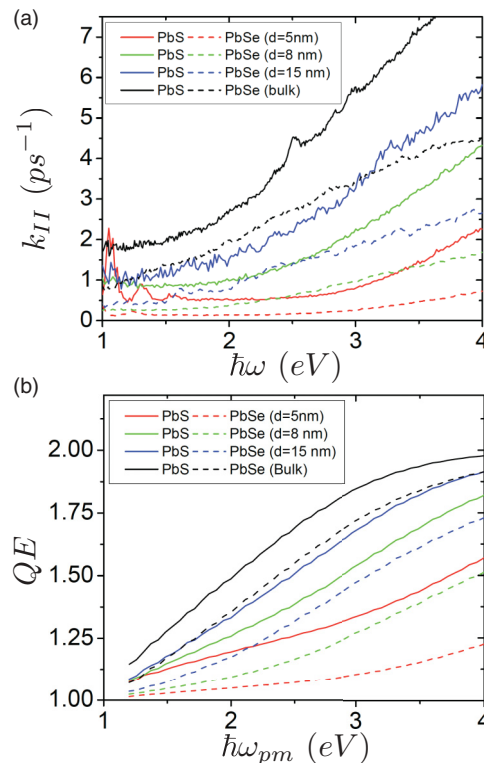

FIG. 12. (Color online) Energy dependence of (a) impact ionization rate and (b) total QE calculated for PbS (solid lines) and PbSe (dash) nanocrystals, and the bulk. For all curves in (b), the phonon-assisted relaxation time is set to $\tau_{\mathrm{ph}} = 1.0$ ps.

demonstrating that the overall *calculated* QE in PbS is higher than in PbSe. The latter is a result of the interplay between the band gap energies, effective masses and the dielectric constant values as discussed above.

Ultrafast measurements of QE in bulk PbS and PbSe show that QE for both materials are approximately the same.[37] However, the atomistic calculations reported along with the experimental data demonstrate that for identical population decay times (specifically, $\tau_{\mathrm{ph}} = 0.5$ ps) the calculated QE in PbS exceeds that in PbSe. This observation is in direct agreement with our calculations. Taking into account that both models show the same trend in QE for identical population decay times, we conclude that the impact ionization rate in bulk PbS is expected be higher than in PbSe and, consequently, the photogeneration QE. Furthermore, we extend this conclusion to PbS nanocrystals according to the results shown in Fig. 12.

Recently reported ultrafast measurements demonstrated significant reduction in QE of large PbS nanocrystals compared to the PbSe nanocrystals.[83] The authors rationalize this observation by estimating the phonon-assisted energy loss rate which in PbS turns out to be a factor of two faster than in PbSe. A rigorous calculation of the phonon-assisted relaxation is beyond our model capability forcing us to introduce phenomenological τ_{ph}. Since the remaining electronic structure parameters in our and reported atomistic models are well validated, the calculations directly support the idea of the QE reduction in PbS merely due to the fast phonon-assisted population decay characterized by τ_{ph}.

V. DISCUSSION AND CONCLUSIONS

The effective mass model used in this paper has significant limitations accounting only for the L-valley optical transitions.[57] It does not catch contributions from the higher energy transitions originating at other Brillouin zone points. Specifically in PbSe, the Σ-point transitions show large contribution to the absorption spectra above 1.6 eV.[84] Experimentally, the CM dynamics is probed using ultrafast transient absorption and fluorescence techniques.[35] These techniques explicitly determine the number of carriers accumulated near the band edge of the lowest in energy L valley. Following the excitation with a high-energy optical pump, the excitons and biexcitons can be generated not only in L valley (denoted L excitons and biexcitons) but also at Σ point (denoted Σ excitons and biexcitons). The contribution of the Σ excitons to the transient ultrafast signal depends on the mixing between the L and Σ points. Rigorous calculations of the intervalley mixing can be done through atomistic calculations. However, such calculations become tremendously expensive for the considered large diameter nanocrystals. Below, we provide quantitative discussion of possible mixing mechanisms and rough estimates of the their contribution to QE for the pump energy below 3.5 eV.

First, we consider mixing between the valleys due to the size quantization that could be efficient in very small ($d \lesssim 3$ nm) nanocrystals at low excitation energies. However, for the large nanocrystals, considered here, the excitations with the energies higher than 2.5 eV are effectively of the bulk type[84,85] resulting in the negligible quantum-confinement-induced mixing. Another option is the impact ionization event initiated by the optically prepared Σ exciton and resulting in the direct production of an extra L exciton. During this process, the excess energy of the Σ exciton is transferred to create an extra electron-hole pair within L valley. The AET for this process can be roughly estimated as $\text{AET}_{\Sigma L} \approx \text{AET}_L + (E_g^{\Sigma} - E_g^{L}) = 3.3$ eV pointing to an *efficient* CM at photon energies $\hbar\omega_{pm} \gtrsim 4$ eV. Note that efficient CM events fully constrained to Σ point should occur at even higher energies that are above the excitation energy range considered in this paper.

Finally, the optically prepared Σ exciton can participate in the impact ionization event resulting in the creation of an electron-hole pair through the intervalley transition. For instance, a higher energy conduction band electron from Σ point can be transferred to L-valley releasing the excess energy to create an additional electron-hole pair through the L valence to Σ-conduction band transition. As we mentioned above, most of the states involved in efficient CM are of the bulk type with the quasimomentum being a "good" quantum number. Therefore the Coulomb matrix elements describing the impact ionization processes become $\sim 1/|\Delta\boldsymbol{q}|^2$, where $\Delta\boldsymbol{q}$ is the difference between the electron/hole initial and final states. Accordingly, the impact ionization events involving the intervalley transitions require large variation in the quasimomentum $\Delta\boldsymbol{q}$ and, therefore, become less favorable.

Experimental verification of the discussed interplay between the CM pathways contributing to the photogeneration QE requires direct measurements of the interband Coulomb interactions. Distinguishing the inter- and intraband Coulomb interactions is a challenging task, since in the transient absorption and time-resolved fluorescence experiments these two components contribute to a measured energy shift between the exciton and biexciton bands. We have shown theoretically that the two-dimensional double-quantum coherence spectroscopy is capable to probe directly the interband Coulomb interactions.[86] Alternatively, the photogeneration QE can be determined based on its linear relationship to the impact ionization rate which has been established above [see Eq. (30)]. The later rate can be obtained by fitting the total QE as a function of the excitation energy.[87] However, the determination of the effective dephasing rate, also entering Eq. (30), might require use of coherent experimental technique (e.g., photon echo) and/or modeling of the phonon-induced relaxation processes.

The absolute photon energy scale $\hbar\omega_{pm}$ is used throughout this paper [except Fig. 3(a) and 8]. This scale is more useful to discuss fundamental physical mechanisms determining the CM dynamics, e.g., the role of the quantum confinement.[25,64] However, performance of photovoltaic devices can be characterized by various power conversion efficiencies.[35,64] In particular, QE can be calculated on a dimensionless energy scale, which is normalized per nanocrystal or bulk band gap, $\hbar\omega_{pm}/E_g$. Despite lower values of QE in nanocrystals compared to the bulk that show up on the absolute photon energy scale, the performance of prospective photovoltaic devices based on nanocrystals can overrun their bulk counterpart.[36,64,87] By comparing Fig. 8 with Fig. 7(b), one can notice that smaller size nanocrystals have better rise in QE than large ones and the bulk. This results from the quantum-confinement-induced blue shift of the band gap energy.[45] In light of this effect and the requirement to match solar radiation peak energy, semimetal nanocrystals can become more efficient solar energy converters.[88]

Further enhancement of the interband Coulomb interactions in nanocrystals can possibly be reached in nanocrystal-metal heterostructures in which the surface plasmon response is tuned in resonance with the exciton states participating in CM. This issue requires additional study, since besides the enhancement of the Coulomb interactions, the surface-plasmons-induced Ohmic and radiative energy losses can become significant.[89] The large variations in the experimentally observed QE including total suppression of CM processes or their additional enhancement are likely due to the the surface states and ligands. This question is difficult to analyze using the adopted effective mass approximation. However, the atomistic calculations[30,31,63,90–92] combined with the interband exciton scattering model should be extremely helpful in addressing this issue.

In conclusion, we have performed a systematic numerical investigation of CM mechanisms in nanocrystalline and bulk PbSe and PbS using our interband exciton scattering model parametrized by the effective mass Kang-Wise model. We investigated the role of quantum confinement in the photogeneration and total QE. The analysis of the photogeneration pathways resulted in an unexpected conclusion that the photogeneration processes reduce to a single impact ionization event due to the complete lack of the pathways interference. This allowed us to explain the minor role of the photogeneration in the net QE dominated by the multiple

impact ionization events occurring during the phonon-assisted population decay. Comparison of the size scaling of the effective Coulomb interaction and the biexciton DOS in transition from nanocrystal to the bulk limit showed that the weak enhancement of the former quantity is overrun by a significant reduction in the latter one. This explains the higher values of the QE in bulk compared to nanocrystals as plotted on the absolute energy scale, and well agrees with the previously reported experimental studies and some theoretical predictions. However, the quantum-confinement-induced increase in E_g makes nanocrystals more efficient than bulk for practical photovoltaic applications. We have also found that the variation in the pump pulse duration does not significantly change the QE. Comparison of QE in PbSe and PbS suggests that the impact ionization processes are more efficient in PbS. However, variation of the material-dependent population decay time can strongly affect the total QE. Finally, we have identified the limitations of our model and defined its applicability range.

APPENDIX A: INTERBAND EXCITON SCATTERING MODEL IN THE WEAK COULOMB COUPLING LIMIT

In this appendix, we derive leading contributions to the photogenerated exciton and biexciton populations and the kinetic equations describing their further phonon-assisted relaxation. Our derivation is based on a simple perturbation expansion, valid in the weak interband Coulomb coupling regime. For the sake of simplicity, the calculations are not rigorous. One can find a complete analysis of the weak Coulomb coupling limit of the interband exciton scattering model including the terms omitted below in Ref. 48.

Let us consider an ensemble of nanocrystals in which the carrier dynamics is restricted to the coupled exciton and biexciton bands described by the following Hamiltonian:[48]

$$\hat{H} = \hat{H}_0 + \hat{V}_C. \tag{A1}$$

Here, the first term,

$$\hat{H}_0 = \sum_{a \geqslant 1} |x_a\rangle \hbar \omega_a^x \langle x_a| + \sum_{k \geqslant 1} |xx_k\rangle \hbar \omega_k^{xx} \langle xx_k|, \tag{A2}$$

describes noninteracting exciton $|x_a\rangle$ and biexciton $|xx_k\rangle$ states and the second term,

$$\hat{V}_C = \sum_{a \geqslant 0} \sum_{k \geqslant 1} |x_a\rangle V_{a,k}^{x,xx} \langle xx_k| + \text{H.c.}, \tag{A3}$$

represents the interband Coulomb interactions $V_{a,k}^{x,xx}$ between the exciton and biexciton states as well as the ground state, $|x_0\rangle$, to biexciton states couplings, $V_{k,0}^{xx,x}$. Details on the calculations of these matrix elements in the Kang-Wise basis are given in Appendix C.

In the weak Coulomb coupling limit of our interband exciton scattering model, we account for the Born scattering between the exciton and biexciton bands. This is equivalent to the calculation of the eigenstates of the total Hamiltonian, Eqs. (A1)–(A3), (i.e., dressed exciton $|\tilde{x}_a\rangle$ and biexciton $|\widetilde{xx}_k\rangle$ states) by using the first-order perturbation expansion in V_C,[93,94]

$$|\tilde{x}_a\rangle = |x_a\rangle + \Lambda_{a,k}^{x,xx} |xx_k\rangle, \tag{A4}$$

$$|\widetilde{xx}_k\rangle = |xx_k\rangle + \Lambda_{k,a}^{xx,x} |x_a\rangle. \tag{A5}$$

Here, $\Lambda_{a,k}^{x,xx} = \Lambda_{k,a}^{xx,x}$ is given by Eq. (5) with the dephasing rate $\gamma_{a,k}^{x,xx}$ added to account for the level broadening.

The exciton/biexciton dipole coupling to the time-dependent optical field is described by the Hamiltonian[95]

$$\hat{H}_{\text{int}}(t) = -\hat{\mu}E(t). \tag{A6}$$

Here, $\hat{\mu}$ is the dipole operator projected on the direction of the linearly polarized pump pulse whose electric field amplitude is

$$E(\mathbf{r},t) = \mathcal{E}_{pm}(t)e^{i\mathbf{k}_{pm}\cdot\mathbf{r}-i\omega_{pm}t} + \text{c.c.} \tag{A7}$$

$\mathcal{E}_{pm}(t)$ is the pump pulse time-depended envelope function and ω_{pm} ($\mathbf{k}_{pm}$) is the pulse central frequency (wave vector).

To find the pump induced (i.e., photogenerated) populations, one needs to solve the following Liouville equation:

$$\dot{\rho}(t) = \frac{1}{i\hbar}[\hat{H} + \hat{H}_{\text{int}}(t), \hat{\rho}(t)], \tag{A8}$$

for the density operator $\hat{\rho}(t)$. Throughout this Appendix, brackets denote the commutator. By considering the Hamiltonian, $H_{\text{int}}(t)$, as a perturbation, the second-order solution of Eq. (A8),

$$\hat{\tilde{\rho}}(t) = \frac{1}{(i\hbar)^2} \int_{-\infty}^{\infty} dt' \int_{-\infty}^{\infty} dt''$$
$$\times \theta(t - t')\theta(t' - t'')[\hat{\tilde{H}}_{\text{int}}(t'), [\hat{\tilde{H}}_{\text{int}}(t''), \hat{\rho}_{\text{eq}}]], \tag{A9}$$

gives the lowest-order contribution to the photoinduced populations.[95] In Eq. (A9), $\hat{\tilde{\rho}}(t) = e^{i\hat{H}t/\hbar}\hat{\rho}(t)e^{-i\hat{H}t/\hbar}$ and $\hat{\tilde{H}}_{\text{int}}(t) = e^{i\hat{H}t/\hbar}\hat{H}_{\text{int}}(t)e^{-i\hat{H}t/\hbar}$ are the density operator and the optical coupling Hamiltonian represented in the interaction picture, respectively. The equilibrium density operator, $\hat{\rho}_{\text{eq}} = |\tilde{x}_0\rangle\langle\tilde{x}_0|$, is projection operator on the dressed ground state defined in Eq. (A4) by setting $a = 0$.

According to Eq. (A9), the populations of the dressed exciton and biexciton states at times longer than the pulse duration calculated in the rotating wave approximation[95] are

$$\langle\tilde{x}_a|\hat{\rho}|\tilde{x}_a\rangle = \frac{2}{\hbar^2}|\langle\tilde{x}_a|\hat{\mu}|\tilde{x}_0\rangle|^2 \mathcal{I}(\omega_a^x - \omega_{pm}), \tag{A10}$$

$$\langle\widetilde{xx}_k|\hat{\rho}|\widetilde{xx}_k\rangle = \frac{2}{\hbar^2}|\langle\widetilde{xx}_k|\hat{\mu}|\tilde{x}_0\rangle|^2 \mathcal{I}(\omega_k^{xx} - \omega_{pm}), \tag{A11}$$

respectively. In Eqs. (A10) and (A11), the pulse self-convolution function has the form given by Eq. (3) with the time variable $t_1 = t' - t''$, and the phenomenologically added

dephasing rates γ_a^x and γ_k^{xx}. According to Eqs. (A4) and (A5), the transition dipole matrix elements entering Eqs. (A10) and (A11) become

$$\langle \tilde{x}_a | \hat{\mu} | \tilde{x}_0 \rangle = \mu_{a0}^x + \sum_{kl \geqslant 1} \Lambda_{a,k}^{x,xx} \mu_{kl}^{xx} \Lambda_{l,0}^{xx,x}, \qquad \text{(A12)}$$

$$\langle \widetilde{xx}_k | \hat{\mu} | \tilde{x}_0 \rangle = \sum_{l \geqslant 1} \mu_{kl}^{xx} \Lambda_{l,0}^{xx,x} + \sum_{a \geqslant 1} \Lambda_{k,a}^{xx,x} \mu_{a0}^x, \quad \text{(A13)}$$

and depend on the intraband exciton and biexciton transition dipole matrix elements μ_{a0}^x and μ_{kl}^{xx} represented in the noninteracting exciton and biexciton basis. Their further calculation in the Kang-Wise basis set is outlined in Appendix C. We have validated numerically that the contributions of the transition dipoles between exciton and biexciton bands is negligible and therefore, do not include the associated terms into Eqs. (A10) and (A11).

Finally, the exciton, n_a^x, and biexciton, n_k^{xx}, populations used in our numerical simulations can be obtained by transforming Eqs. (A10) and (A11) back to the noninteracting exciton and biexciton basis. Specifically,

$$n_a^x = \sum_{b \geqslant 1} |\langle x_a | \tilde{x}_b \rangle|^2 \langle \tilde{x}_b | \hat{\rho} | \tilde{x}_b \rangle$$
$$+ \sum_{k \geqslant 1} |\langle x_a | \widetilde{xx}_k \rangle|^2 \langle \widetilde{xx}_k | \hat{\rho} | \widetilde{xx}_k \rangle, \qquad \text{(A14)}$$

$$n_k^{xx} = \sum_{a \geqslant 1} |\langle xx_k | \tilde{x}_a \rangle|^2 \langle \tilde{x}_a | \hat{\rho} | \tilde{x}_a \rangle$$
$$+ \sum_{l \geqslant 1} |\langle xx_k | \widetilde{xx}_l \rangle|^2 \langle \widetilde{xx}_l | \hat{\rho} | \widetilde{xx}_l \rangle. \qquad \text{(A15)}$$

By calculating the transformation coefficients according to Eqs. (A4) and (A5) and further inserting them into Eq. (A15), one finds the lowest, second order in $\Lambda_{a,k}^{x,xx}$, contribution to the biexciton population given by Eq. (4). The calculation of the exciton population up to the second-order terms in $\Lambda_{a,k}^{x,xx}$, can be done by accounting for the second-order interband scattering events, [i.e., the second-order corrections not included into Eqs. (A4) and (A5)].[48] However, our numerical calculations have shown that these terms provide negligible contribution to the photogeneration QE and one can safely use the leading term given by Eq. (2), which naturally follows from Eq. (A14) as the zero-order contribution. Finally, we have neglected the contributions of the density matrix coherences, $\langle \tilde{x}_a | \hat{\rho} | \tilde{x}_b \rangle$ with $a \neq b$, $\langle \widetilde{xx}_k | \hat{\rho} | \widetilde{xx}_l \rangle$ with $k \neq l$, and $\langle \tilde{x}_a | \hat{\rho} | \widetilde{xx}_k \rangle$ to the photogenerated populations[48] based on their negligible contribution to the photogeneration QE as validated numerically.

The photogenerated populations [Eqs. (2) and (4)] further evolve on the longer time scale associated with the phonon-assisted processes. This dynamics can be described by the following Liouville equation:

$$\dot{\rho}(t) = \frac{1}{i\hbar}[\hat{H}, \rho(t)] + \hat{\Gamma} \rho(t), \qquad \text{(A16)}$$

where $\hat{H}$ is the Hamiltonian given by Eqs. (A1)–(A3) and $\hat{\Gamma}$ is the Liouville space relaxation operator describing the phonon-assisted dephasing and population decay processes.[68,95]

By taking the matrix elements of Eq. (A16) for the exciton, $n_a^x = \langle x_a | \hat{\rho}(t) | x_a \rangle$, and biexciton, $n_k^{xx} = \langle xx_k | \hat{\rho}(t) | xx_k \rangle$, state populations, one obtains the following set of equations:

$$\dot{n}_a^x = \frac{1}{i\hbar} \sum_m V_{a,m}^{x,xx} \left(\rho_{m,a}^{xx,x} - \rho_{a,m}^{x,xx} \right)$$
$$- \sum_b \left(\Gamma_{ba}^x n_a^x - \Gamma_{ab}^x n_b^x \right), \qquad \text{(A17)}$$

$$\dot{n}_k^{xx} = \frac{1}{i\hbar} \sum_b V_{b,k}^{x,xx} \left(\rho_{b,k}^{x,xx} - \rho_{k,b}^{xx,x} \right)$$
$$- \sum_m \left(\Gamma_{mk}^{xx} n_k^{xx} - \Gamma_{km}^{xx} n_m^{xx} \right), \qquad \text{(A18)}$$

containing matrix elements, Γ_{ba}^x and Γ_{km}^{xx}, of the relaxation operator, $\hat{\Gamma}$, standing for the phonon-assisted intraband population decay rates, respectively. We have demonstrated that in the weak electron-phonon coupling regime, the phonon-assisted processes do not mix the exciton and biexciton bands[48] and therefore do not include these processes into Eqs. (A17) and (A18).

Equations (A17) and (A18) should be complimented by the equation for the interband coherences, $\rho_{a,k}^{x,xx} = \langle x_a | \hat{\rho}(t) | xx_k \rangle$, which according to Eq. (A16) read

$$\dot{\rho}_{a,k}^{x,xx} + i \left(\omega_a^x - \omega_k^{xx} + i\gamma_{a,n}^{x,xx} \right) \rho_{a,k}^{x,xx} = \frac{1}{i\hbar} V_{a,k}^{x,xx} \left(n_k^{xx} - n_a^x \right). \qquad \text{(A19)}$$

Here, we dropped the terms containing the intraband exciton and biexciton coherences giving negligible corrections to ω_a^x and ω_k^{xx}. $\gamma_{a,n}^{x,xx}$ is the matrix element of the phonon-assisted relaxation operator describing the pure dephasing processes.[95]

Taking into account that the population decay dynamics occurs on the time scale larger than the dephasing processes, Eq. (A19) can be integrated using the Markovian approximation. Further eliminating the coherences in Eqs. (A17) and (A18), one finds the following set of kinetic equations for the phonon-assisted intraband population decay accompanied by the impact ionization and Auger recombination processes:

$$\dot{n}_a^x = - \sum_m k_{a,m}^{x,xx} \left(n_a^x - n_m^{xx} \right)$$
$$- \sum_b \left(\Gamma_{ba}^x n_a^x - \Gamma_{ab}^x n_b^x \right), \qquad \text{(A20)}$$

$$\dot{n}_k^{xx} = - \sum_b k_{b,k}^{x,xx} \left(n_k^{xx} - n_b^x \right)$$
$$- \sum_m \left(\Gamma_{mk}^{xx} n_k^{xx} - \Gamma_{km}^{xx} n_m^{xx} \right). \qquad \text{(A21)}$$

Here, the interband population transfer rate in the limit $\gamma_{a,k}^{x,xx} \to 0$ is

$$k_{a,n}^{x,xx} = \frac{2\pi}{\hbar^2} \left| V_{a,k}^{x,xx} \right|^2 \delta \left(\omega_a^x - \omega_k^{xx} \right). \qquad \text{(A22)}$$

This rate gives rise to the impact ionization and Auger recombination rates after the convolution with the biexciton and exciton DOS, respectively.

This rate gives rise to the impact ionization and Auger recombination rates after the convolution with the biexciton and exciton DOS, respectively.

APPENDIX B: VOLUME SCALINGS OF DOS, TRANSITION DIPOLES, AND THE EFFECTIVE COULOMB INTERACTION

In this appendix, we derive the volume normalization prefactors entering Eqs. (11)–(16). The prefactors cancel out the volume dependence of the latter quantities making them intensive variables in the bulk (i.e., thermodynamic) limit. To preserve the dimensionality of the intensive variables, we use the V/v ratio instead of V, where v is the unit cell volume. This ratio defines number of unit cells and goes to infinity in the bulk limit. Here, we also use the relationships derived in Appendix C that connect the transition dipole movements and Coulomb matrix elements represented in the single-particle Kanf-Wise basis set and in the exciton/biexciton basis.

We start with the simple fact that in the bulk limit, the single-particle DOS is proportional to the system volume V.[96] Defining the exciton (biexciton) DOS as a joint DOS of uncorrelated electron and hole (uncorrelaed two electrons and two holes), one immediately finds that they have V^2 (V^4) scalings. Therefore we introduced the v^2/V^2 (v^4/V^4) prefactor into Eq. (11) [Eq. (12)].

To obtain the volume prefactors in the optically allowed DOS given by Eqs. (13) and (14), we first notice that the transition dipole matrix element for a single carrier has no volume scaling and accounts for the total momentum conservation, i.e., $M_{ij} \sim V^0 M_{\mathbf{k}_i,\mathbf{k}_j} \delta_{\mathbf{k}_i,\mathbf{k}_j}$.[97] Further using Eq. (C2), we find that the optically allowed exciton DOS scales as

$$\sum_a |\mu_{a0}^x|^2 \delta(\omega - \omega_a^x) \sim \sum_{\mathbf{k}_p} |M_{\mathbf{k}_p,\mathbf{k}_p}^{eh}|^2 \delta(\omega - \omega_{\mathbf{k}_p}^e - \omega_{\mathbf{k}_p}^h) \sim V.$$

$$(B1)$$

Here and below, we use the same argument as in the DOS analysis that for a fixed energy interval, $\sum_{\mathbf{k}_p} \sim V$. Using the first term in the expansion of the intraband biexciton dipole moment given by Eq. (C3), one finds that the joint optically allowed biexciton DOS scales as

$$\sum_{kl} |\mu_{kl}^{xx}|^2 \delta(\omega_1 - \omega_k^{xx}) \delta(\omega_2 - \omega_l^{xx})$$
$$\sim \sum_{\mathbf{k}_p \mathbf{k}_q} \sum_{\mathbf{k}_r \mathbf{k}_s} |M_{\mathbf{k}_p,\mathbf{k}_p}^{ee}|^2 \delta(\omega_1 - \omega_{\mathbf{k}_p}^e - \omega_{\mathbf{k}_q}^e - \omega_{\mathbf{k}_r}^h - \omega_{\mathbf{k}_s}^h)$$
$$\times \delta(\omega_2 - \omega_{\mathbf{k}_p}^{e'} - \omega_{\mathbf{k}_q}^e - \omega_{\mathbf{k}_r}^h - \omega_{\mathbf{k}_s}^h) \sim V^4. \quad (B2)$$

According to Eqs. (B1) and (B2), we introduced the prefactors v/V and $(v/V)^4$ into Eqs. (13) and (14), respectively.

To determine the volume scaling of the effective Coulomb term [see Eq. (15)], we first evaluate the scaling of the following auxiliary quantity:

$$\mathcal{K}(\omega_1, \omega_2) = \sum_{a,m} |V_{a,m}^{x,xx}|^2 \delta(\omega_1 - \omega_a^x) \delta(\omega_2 - \omega_m^{xx}). \quad (B3)$$

According to Eq. (C10), the Coulomb matrix elements in the free carriers basis scales as $V_{ij,kl} \sim V^{-1} V_{\mathbf{k}_i \mathbf{k}_j, \mathbf{k}_k \mathbf{k}_l} \delta_{\mathbf{k}_i - \mathbf{k}_l, \mathbf{k}_j - \mathbf{k}_k}$.

Then using Eq. (C6), one finds that

$$\mathcal{K}(\omega_1, \omega_2) \sim V^{-2} \sum_{\mathbf{k}_i \mathbf{k}_j \mathbf{k}_k \mathbf{k}_l} |V_{\mathbf{k}_i,\mathbf{k}_j,\mathbf{k}_k,\mathbf{k}_i+\mathbf{k}_j+\mathbf{k}_k}^{eehe}|^2$$
$$\times \delta(\omega_2 - \omega_{\mathbf{k}_i}^e - \omega_{\mathbf{k}_j}^e - \omega_{\mathbf{k}_k}^h - \omega_{\mathbf{k}_l}^h)$$
$$\times \delta(\omega_1 - \omega_{\mathbf{k}_i+\mathbf{k}_j-\mathbf{k}_k}^e - \omega_{\mathbf{k}_l}^h) \sim V^2. \quad (B4)$$

By taking into account that $\mathcal{K}$ should be normalized by the exciton and biexciton DOS and take square root, we introduce the prefactor $(V/v)^2$ into Eq. (15). The volume prefactor in Eq. (16) can be obtained in the same way with the help of Eqs. (C5), (C10), and (C11).

APPENDIX C: REPRESENTATION OF TRANSITION DIPOLES AND INTERBAND COULOMB MATRIX ELEMENTS IN KANG-WISE BASIS SET

In this appendix, we provide closed expressions for the exciton and biexciton transition dipoles and the interband Coulomb matrix elements used in the numerical calculations. To derive these expressions, we follow the procedure outlined in Appendices A–C of Ref. 48.

The second quantization is performed using the basis of Kang-Wise states, $\{\Psi_i(\mathbf{r})\}$ defined in Eq. (26), by introducing the following field operators:

$$\hat{\Psi}(\mathbf{r}) = \sum_i [\Theta(E_i)\Psi_i(\mathbf{r})c_i + \Theta(-E_i)\Psi_i(\mathbf{r})d_i^\dagger],$$
$$\hat{\Psi}^\dagger(\mathbf{r}) = \sum_i [\Theta(E_i)\Psi_i^*(\mathbf{r})c_i^\dagger + \Theta(-E_i)\Psi_i^*(\mathbf{r})d_i],$$
$$(C1)$$

where $\Theta(E)$ is the step function, c_i and d_i ($c_i^\dagger$ and $d_i^\dagger$) are conduction band electron and valence band hole annihilation (creation) operators, respectively.

Using this representation and the definition of the exciton and biexciton states given by Eqs. (27) and (28), it is straightforward to show that the transition matrix elements entering Eqs. (2) and (4) are

$$\mu_{a0}^x = \langle x_a|\hat{\mathbf{M}}|x_0\rangle = \mathbf{M}_{qr}^{eh}, \quad (C2)$$
$$\mu_{kl}^{xx} = \langle xx_k|\hat{\mathbf{M}}|xx_l\rangle = [\delta_{rr'}\delta_{ss'} - \delta_{rs'}\delta_{r's}]$$
$$\times [\mathbf{M}_{p'p}^{ee}\delta_{qq'} - \mathbf{M}_{q'p}^{ee}\delta_{qp'} - \mathbf{M}_{p'q}^{ee}\delta_{pq'} + \mathbf{M}_{q'q}^{ee}\delta_{pp'}],$$
$$+ [\delta_{pp'}\delta_{qq'} - \delta_{pq'}\delta_{p'q}]$$
$$\times [\mathbf{M}_{s's}^{hh}\delta_{rr'} - \mathbf{M}_{s'r}^{hh}\delta_{sr'} - \mathbf{M}_{r's}^{hh}\delta_{rs'} + \mathbf{M}_{r'r}^{hh}\delta_{ss'}], \quad (C3)$$

respectively. In Eq. (C2), the exciton index $a = \{q,r\}$ and $\mathbf{M}_{qr}^{eh}$ is the interband electron-hole transition dipole matrix element calculated in the Kang-Wise basis set. In Eq. (C3), the biexciton indices are $k = \{p'q',r's'\}$ and $l = \{pq,rs\}$ as well as $\mathbf{M}_{ij}^{ee}$ and $\mathbf{M}_{ij}^{hh}$ are the matrix elements of the intraband transition dipole operator calculated using the electron and hole Kang-Wise wave functions, respectively.

In the envelope function approximation, the Kang-Wise transition matrix elements entering Eqs. (C2) and (C3) have

the following generic form:[57]

$$\mathbf{M}_{ij} = \mathbf{M}_{ij}^{(1)} + \mathbf{M}_{ij}^{(2)},$$

$$\mathbf{M}_{ij}^{(1)} = \sum_{m=1}^{4} \int d\mathbf{r} \left[F_m^i(\mathbf{r}) \right]^* \hat{\mathbf{p}} F_m^j(\mathbf{r}),$$

$$\mathbf{M}_{ij}^{(2)} = P_l \mathbf{z} \int d\mathbf{r} \big\{ \left[F_1^i(\mathbf{r}) \right]^* F_3^j(\mathbf{r}) + \left[F_3^i(\mathbf{r}) \right]^* F_1^j(\mathbf{r}) \\
- \left[F_2^i(\mathbf{r}) \right]^* F_4^j(\mathbf{r}) - \left[F_4^i(\mathbf{r}) \right]^* F_2^j(\mathbf{r}) \big\}, \quad (C4)$$

where the indices i, j denote the electron and hole states, and $\hat{\mathbf{p}} = -i\hbar\nabla$. P_l stands for the longitudinal dipole moment component of the band-edge Bloch function $u_m(\mathbf{r})$ and $\mathbf{z}$ is the unit vector in $\langle 111 \rangle$ direction of the PbSe (PbS) lattice. Both $\mathbf{M}^{(1)}$ and $\mathbf{M}^{(2)}$ can be evaluated analytically in the bulk limit, where $\mathbf{M}^{(1)}$ vanishes identically.[101] Using the same approach as above, one can show that the Coulomb matrix elements entering Eqs. (5), (15), (16), and (B4) are

$$V_{l,0}^{xx,0} = \langle xx_l | \hat{V} | x_0 \rangle = V_{pqrs}^{eehh} - V_{pqsr}^{eehh}, \quad (C5)$$

$$V_{k,a}^{xx,x} = \langle xx_k | \hat{V} | x_a \rangle = \left(V_{q'p'r'q}^{eehe} - V_{p'q'r'q}^{eehe} \right) \delta_{s',r} \\
+ \left(V_{q'p'qs'}^{eeeh} - V_{p'q'qs'}^{eeeh} \right) \delta_{r',r} \\
+ \left(V_{q'rs'r'}^{ehhh} - V_{q'rr's'}^{ehhh} \right) \delta_{p',q} \\
+ \left(V_{p'rr's'}^{ehhh} - V_{p'rr's'}^{ehhh} \right) \delta_{q',q}. \quad (C6)$$

These quantities depend on the long-range contributions whose matrix elements in the Kang-Wise basis read

$$V_{ijkl} = \iint d\mathbf{r}_1 d\mathbf{r}_2 \frac{e^2}{\epsilon |\mathbf{r}_1 - \mathbf{r}_2|} \sum_{m=1}^{4} \left[F_m^i(\mathbf{r}_1) \right]^* F_m^l(\mathbf{r}_1) \\
\times \sum_{n=1}^{4} \left[F_n^j(\mathbf{r}_2) \right]^* F_n^k(\mathbf{r}_2). \quad (C7)$$

Here, ϵ denotes the screened dielectric function values evaluated at the optical frequencies. For bulk PbSe and PbS, we set $\epsilon^{\text{bulk}} = 23$ and 17, respectively.[57] The dielectric constant in the nanocrystals has been evaluated using the following expression:[98]

$$\epsilon^{NC}(d) = 1 + (\epsilon^{\text{bulk}} - 1) \frac{\left(E_g^{\text{bulk}} + \Delta E \right)^2}{\left[E_g^{NC}(d) + \Delta E \right]^2}, \quad (C8)$$

where $E_g^{\text{bulk}} + \Delta E = 2.73$ and 3.14 eV are the energy of the first pronounced absorption peak in the bulk PbSe and PbS, respectively.[99,100]

To derive the volume scaling of the Coulomb matrix elements given by Eq. (C7), we assume the bulk limit in which the envelope functions become plane waves, i.e., $F_m^i(\mathbf{r}_1) = F_m^i e^{i\mathbf{k}_i \mathbf{r}_1}/\sqrt{V}$. In this basis, the Coulomb matrix elements can be written as

$$V_{ijkl} = \frac{e^2}{\epsilon V^2} \sum_{m,n} \left[F_m^i F_n^j \right]^* F_m^l F_n^k \\
\times \iint d\mathbf{r}_1 d\mathbf{r}_2 \frac{1}{|\mathbf{r}_1 - \mathbf{r}_2|} e^{-i\mathbf{k}_i\mathbf{r}_1 - i\mathbf{k}_j\mathbf{k}_2 + i\mathbf{k}_k\mathbf{r}_2 + i\mathbf{k}_l\mathbf{r}_1}. \quad (C9)$$

The integral evaluation leads to the final expression

$$V_{ijkl} = \frac{1}{V^2} V_{\mathbf{k}_i, \mathbf{k}_j, \mathbf{k}_k, \mathbf{k}_l} V \delta_{\mathbf{k}_i - \mathbf{k}_l, \mathbf{k}_j - \mathbf{k}_k}, \quad (C10)$$

where

$$V_{\mathbf{k}_i, \mathbf{k}_j, \mathbf{k}_k, \mathbf{k}_l} = \frac{e^2}{\epsilon} \sum_{m,n} \left[F_m^i F_n^j \right]^* F_m^l F_n^k \frac{4\pi}{|\mathbf{k}_i - \mathbf{k}_l|^2}. \quad (C11)$$

Equations (C10) and (C11) clearly demonstrate a general property that the Coulomb matrix elements used in the numerical calculations of the bulk limit scale inversely proportional to the volume.[97]

The nonparabolicity in the employed $\mathbf{k} \cdot \mathbf{p}$ Hamiltonian is crucial for the accurate evaluation of the above Coulomb matrix elements. Specifically, summations over the spinor components in Eq. (C7) imply that the interband Coulomb scattering amplitudes vanish exactly if the nondiagonal terms of the $\mathbf{k} \cdot \mathbf{p}$ Hamiltonian are set to zero, i.e., in the strictly parabolic case.[80] In the bulk, where the quasimomentum k is a "good" quantum number, diagonal and off-diagonal matrix elements of the $\mathbf{k} \cdot \mathbf{p}$ Hamiltonian scale as k^2 and k, respectively. At high energies, where the diagonal elements dominate over the off-diagonal ones, the latter can be treated perturbatively giving $k^{-1} \sim \omega^{-1/2}$ as the contribution of the hole (electron) states to a high-energy electron (hole) wave function.

---

*kirill@lanl.gov

†apiryat@lanl.gov

[1] S. Kolodinski, J. Werner, T. Wittchen, and H. Queisser, Appl. Phys. Lett. **63**, 2405 (1993).

[2] A. J. Nozik, Physica E **14**, 115 (2002).

[3] R. D. Schaller and V. I. Klimov, Phys. Rev. Lett. **92**, 186601 (2004).

[4] M. Hanna and A. Nozik, J. Appl. Phys. **100**, 074510 (2006).

[5] V. I. Klimov, Appl. Phys. Lett. **89**, 123118 (2006).

[6] M. C. Beard and R. J. Ellingson, Laser and Photon. Rev. **2**, 377 (2008).

[7] A. J. Nozik, Chem. Phys. Lett. **457**, 3 (2008).

[8] J. M. Luther et al., Nano Lett. **8**, 3488 (2008).

[9] S. Koc, Czech. J. Phys. **7**, 91 (1957).

[10] A. Smith and D. Dutton, J. Opt. Soc. Am. **48**, 1007 (1958).

[11] V. Vavilov, J. Phys. Chem. Solids **8**, 223 (1959).

[12] J. Tauc, J. Phys. Chem. Solids **8**, 219 (1959).

[13] O. Christensen, J. Appl. Phys. **47**, 689 (1976).

[14] R. J. Ellingson et al., Nano Lett. **5**, 865 (2005).

[15] R. D. Schaller, V. M. Agranovich, and V. I. Klimov, Nat. Phys. **1**, 189 (2005).

[16] R. D. Schaller, M. A. Petruska, and V. I. Klimov, Appl. Phys. Lett. **87**, 253102 (2005).

[17] R. D. Schaller, M. Sykora, J. M. Pietryga, and V. I. Klimov, Nano Lett. **6**, 424 (2006).

[18] R. D. Schaller and V. I. Klimov, Phys. Rev. Lett. **96**, 097402 (2006).

[19] R. D. Schaller, M. Sykora, S. Jeong, and V. I. Klimov, J. Phys. Chem. B **110**, 25332 (2006).

[20] J. E. Murphy *et al.*, J. Am. Chem. Soc. **128**, 3241 (2006).

[21] R. D. Schaller, J. M. Pietryga, and V. I. Klimov, Nano Lett. **7**, 3469 (2007).

[22] M. C. Beard *et al.*, Nano Lett. **7**, 2506 (2007).

[23] J. J. H. Pijpers *et al.*, J. Phys. Chem. C **111**, 4146 (2007).

[24] G. Nair and M. G. Bawendi, Phys. Rev. B **76**, 081304(R) (2007).

[25] G. Nair, S. M. Geyer, L.-Y. Chang, and M. G. Bawendi, Phys. Rev. B **78**, 125325 (2008).

[26] M. Ben-Lulu *et al.*, Nano Lett. **8**, 1207 (2008).

[27] J. J. H. Pijpers *et al.*, J. Phys. Chem. C **112**, 4783 (2008).

[28] A. Franceschetti and Y. Zhang, Phys. Rev. Lett. **100**, 136805 (2008).

[29] M. C. Beard *et al.*, Nano Lett. **9**, 836 (2009).

[30] S. Kilina, S. Ivanov, and S. Tretiak, J. Am. Chem. Soc. **131**, 7717 (2009).

[31] G. Allan and C. Delerue, Phys. Rev. B **79**, 195324 (2009).

[32] P. Tyagi and P. Kambhampati, J. Chem. Phys. **134**, 094706 (2011).

[33] G. Nootz, L. A. Padilha, L. Levina, V. Sukhovatkin, S. Webster, L. Brzozowski, E. H. Sargent, D. J. Hagan, and E. W. VanStryland, Phys. Rev. B **83**, 155302 (2011).

[34] I. Gdor *et al.*, ACS Nano **6**, 3269 (2012).

[35] J. A. McGuire *et al.*, Acc. Chem. Res. **41**, 1810 (2008).

[36] J. A. McGuire *et al.*, Nano Lett. **10**, 2049 (2010).

[37] J. J. H. Pijpers *et al.*, Nat. Phys. **5**, 811 (2009).

[38] M. T. Trinh *et al.*, Nano Lett. **8**, 1713 (2008).

[39] M. Ji *et al.*, Nano Lett. **9**, 1217 (2009).

[40] M. T. Trinh *et al.*, Nano Lett. **11**, 1623 (2011).

[41] O. Roslyak, G. Gumbs, and S. Mukamel, J. Mod. Opt. **57**, 2009 (2010).

[42] O. Roslyak, G. Gumbs, and S. Mukamel, Nano Lett. **10**, 4253 (2010).

[43] J. B. Sambur, T. Novet, and B. A. Parkinson, Science **330**, 63 (2010).

[44] O. E. Semonin *et al.*, Science **334**, 1530 (2011).

[45] G. Nair, J. Zhao, and M. G. Bawendi, Nano Lett. **11**, 1136 (2011).

[46] J. Dai, M. E. Raikh, and T. V. Shahbazyan, Phys. Rev. Lett. **96**, 066803 (2006).

[47] E. Rabani and R. Baer, Chem. Phys. Lett. **496**, 227 (2010).

[48] A. Piryatinski and K. A. Velizhanin, J. Chem. Phys. **133**, 084508 (2010).

[49] E. Antoncik and N. Gaur, J. Phys. D: Solid State Phys. **11**, 735 (1978).

[50] E. Kane, Phys. Rev. **159**, 624 (1967).

[51] P. T. Landsberg, *Recombination in Semiconductors* (Cambridge University Press, New York, 2003).

[52] A. Franceschetti, J. M. An, and A. Zunger, Nano Lett. **6**, 2191 (2006).

[53] E. Rabani and R. Baer, Nano Lett. **8**, 4488 (2008).

[54] G. Allan and C. Delerue, Phys. Rev. B **73**, 205423 (2006).

[55] G. Allan and C. Delerue, Phys. Rev. B **77**, 125340 (2008).

[56] V. I. Rupasov and V. I. Klimov, Phys. Rev. B **76**, 125321 (2007).

[57] I. Kang and F. W. Wise, J. Opt. Soc. Am. B **14**, 1632 (1997).

[58] L. Silvestri and V. M. Agranovich, Phys. Rev. B **81**, 205302 (2010).

[59] A. Shabaev, A. L. Efros, and A. J. Nozik, Nano Lett. **6**, 2856 (2006).

[60] W. M. Witzel, A. Shabaev, C. S. Hellberg, V. L. Jacobs, and A. L. Efros, Phys. Rev. Lett. **105**, 137401 (2010).

[61] O. V. Prezhdo, Acc. Chem. Res. **42**, 2005 (2009).

[62] S. A. Fischer, A. B. Madrid, C. M. Isborn, and O. V. Prezhdo, J. Phys. Chem. Lett. **1**, 232 (2010).

[63] K. Hyeon-Deuk and O. V. Prezhdo, Nano Lett. **11**, 1845 (2011).

[64] C. Delerue, G. Allan, J. J. H. Pijpers, and M. Bonn, Phys. Rev. B **81**, 125306 (2010).

[65] K. A. Velizhanin and A. Piryatinski, Phys. Rev. Lett. **106**, 207401 (2011).

[66] The interband exciton scattering model we use is a complimentary approach to the Hilbert space Green's function method independently proposed by Rabani and Baer.[47] In contrast to our calculations, the latter method has been used along with the atomistic electronic structure model and subsequently applied to the smaller size nanocrystals.

[67] The term is chosen to emphasize that at low DOS, the representation captures discrete level structure making quantities of interest peaked at ω equals to the level energies. However, as the DOS becomes dense, this representation naturally interpolates the quantities of interest as the continuously varying functions of ω.

[68] N. G. V. Kampen, *Stochastic Processes in Physics and Chemistry* (Elsevier, New York, 2008).

[69] Specifically, the numerator in Eq. (15) is the transformation of the discrete Coulomb coupling matrix elements to the quasicontinuous representation resulting in the net Coulomb coupling between the states falling into the frequency intervals $[\omega_1, \omega_1 + d\omega_1]$ and $[\omega_2, \omega_2 + d\omega_2]$. The denominator is the product of the exciton and biexciton DOS given by Eqs. (11) and (12), respectively, with the volume prefactors dropped.

[70] J.-W. Luo, A. Franceschetti, and A. Zunger, Nano Lett. **8**, 3174 (2008).

[71] R. Zwanzig, *Nonequilibrium Statistical Mechanics* (Oxford University Press, New York, 2001).

[72] M. Grifoni, E. Paladino, and U. Weiss, Eur. Phys. J. B **10**, 719 (1999).

[73] D. L. Mitchell and R. F. Wallis, Phys. Rev. **151**, 581 (1966).

[74] J. O. Dimmock, in *The Physics of Semimetals and Narrow Gap Semiconductors*, edited by D. L. Carter and R. T. Bates (Pergamon, Oxford, 1971).

[75] The exception is the calculation of the QE dependence on τ_{pm} where we specifically indicate τ_{pm} variation range.

[76] For $\tau_{pm} > \gamma_{\text{eff}}^{-1}$, the γ_{eff}^{-1} characterizes the time scale of the pump pulse interaction with nanocrystals.

[77] H. Kamisaka, S. V. Kilina, K. Yamashita, and O. V. Prezhdo, Nano Lett. **6**, 2295 (2006).

[78] H. Kamisaka, S. V. Kilina, K. Yamashita, and O. V. Prezhdo, J. Phys. Chem. C **112**, 7800 (2008).

[79] L. V. Keldysh, Sov. Phys. JETP **37**, 509 (1960).

[80] B. K. Ridley, Semicond. Sci. Technol. **2**, 116 (1987).

[81] C. Bonati, A. Cannizzo, D. Tonti, A. Tortschanoff, F. vanMourik, and M. Chergui, Phys. Rev. B **76**, 033304 (2007).

[82] Specifically, the ATE has some energy distribution associated with the 5% diameter variation. However, the E_g used to normalize the photon energy is an averaged value of the band gap energy.

Therefore, the values of QE below *averaged* $2E_g$ are due to the contributions of the subensembles with actual E_g values below its mean value.

[83] J. T. Stewart *et al.*, Nano Lett. **12**, 622 (2012).

[84] R. Koole *et al.*, Small **4**, 127 (2008).

[85] I. Moreels and Z. Hens, Small **4**, 1866 (2008).

[86] K. A. Velizhanin and A. Piryatinski, J. Phys. Chem. B **115**, 5372 (2011).

[87] M. C. Beard *et al.*, Nano Lett. **10**, 3019 (2010).

[88] G. Allan and C. Delerue, ACS Nano **5**, 7318 (2011).

[89] L. Novotny and B. Hecht, *Principles of Nano-Optics* (Cambridge University Press, New York, 2008).

[90] V. V. Albert, S. A. Ivanov, S. Tretiak, and S. V. Kilina, J. Phys. Chem. C **115**, 15793 (2011).

[91] S. A. Fischer *et al.*, Nanoscale **4**, 904 (2012).

[92] S. Kilina *et al.*, ACS Nano **6**, 6515 (2012).

[93] J. J. Sakurai, *Modern Quantum Mechanics* (Addison-Wesley, New York, 1994).

[94] E. N. Economou, *Green's functions in Quantum Physics* (Springer-Verlag, New York, 1983).

[95] S. Mukamel, *Principles of Nonlinear Optical Spectroscopy* (Oxford University Press, Oxford, 1995).

[96] M. Toda, R. Kubo, and N. Saito, *Statistical Physics I*, *Solid-state sciences*, 2nd ed. (Springer, Berlin, 1995).

[97] H. Haug and S. W. Koch, *Quantum Theory of the Optical and Electronic Properties of Semiconductors* (World Scientific, London, 2009).

[98] A. Franceschetti, H. Fu, L. W. Wang, and A. Zunger, Phys. Rev. B **60**, 1819 (1999).

[99] N. Suzuki, K. Sawai, and S. Adachi, J. Appl. Phys. **77**, 1249 (1995).

[100] H. Kanazawa and S. Adachi, J. Appl. Phys. **83**, 5997 (1998).

[101] In the bulk limit, the operator $\hat{\mathbf{p}}$ commutes with the bulk Hamiltonian, and therefore, $\mathbf{M}^{(1)}$ becomes proportional to $\sum_{m=1}^{4} \int d\mathbf{r} [F_m^i(\mathbf{r})]^* F_m^j(\mathbf{r})$, which is zero identically due to the orthogonality of the initial and the final wave functions.